

A continuous time random walk method to predict dissolution in porous media based on validation of experimental NMR data



Rodolfo Oliveira ^{a,*}, Branko Bijeljic ^a, Martin J. Blunt ^a, Adam Colbourne ^{b,c}, Andrew J. Sederman ^b, Mick D. Mantle ^b, Lynn F. Gladden ^b

^a Department of Earth Science and Engineering, Imperial College London, London, UK

^b Department of Chemical Engineering, University of Cambridge, Cambridge, UK

^c Schlumberger Cambridge Research, Cambridge, UK

ARTICLE INFO

Keywords:

Continuous time random walk
Reactive transport modelling
Nuclear magnetic resonance
Dissolution
Carbonate rocks

ABSTRACT

We develop a reactive transport model for dissolution of porous materials using a Continuous Time Random Walk (CTRW) formulation with first-order kinetics. Our model is validated with a dataset for a Ketton carbonate rock sample undergoing dissolution on injection of an acid, monitored using Nuclear Magnetic Resonance (NMR). The experimental data includes the 3D porosity distribution at the beginning and end of the experiment, 1D porosity profiles along the direction of flow during dissolution, as well as the molecular fluid displacement probability distributions (propagators). With the calibration of only a single parameter, we successfully predict the porosity changes and the propagators as a signature of flow heterogeneity evolution in the dissolution experiment.

We also demonstrate that heterogeneity in the flow field leads to an effective reaction rate, limited by transport of reactants, that is almost three orders of magnitude lower than measured under batch reaction conditions. The effective reaction rate predicted by the model is in good agreement with the experimentally measured rate. Furthermore, as dissolution proceeds, the formation of channels in the rock focused the flow in a few fast-flowing regions. The predicted dissolution patterns are similar to those observed experimentally. This study establishes a workflow to calibrate and validate the CTRW reactive transport model with NMR experiments.

1. Introduction

Studies concerning reactive transport in porous media are present in a variety of disciplines and processes including reservoir matrix stimulation (Mahmoud et al., 2017), geological carbon dioxide storage (Metz et al., 2010), and nuclear waste disposal (Kenney et al., 2017), for example. The latest and largest recent oilfield discoveries are formed in carbonate reservoirs (Terra et al., 2010), and deep aquifers within the same sedimentary basins are seen as potential sites for carbon dioxide storage (Bachu, 2003). Such rocks have a complex pore-scale structure (Blunt et al., 2013; Wildenschild and Sheppard, 2013), with geometrical and chemical features that differ significantly from sandstones (Choquette and Pray, 1970); for instance, the permeability of limestone formations can extend over several orders of magnitude (Clerke, 2009) and have a significant amount of interconnected micro- and macro-porosity (Lin et al., 2016). Considering these complexities, it is of great interest to predict dissolution behaviour through developing modelling tools that are validated with experiments.

Computed Tomography (CT) is a commonly used non-destructive technique to image the internal structure of rocks. In addition, Magnetic Resonance Imaging (MRI) is also able to image the fluid distributions and their transport within rocks. Laboratory experiments using MRI have shown the existence of preferential paths controlling transport in porous media (Hoffman et al., 1996; Oswald et al., 1997). Such characteristics, along with the imposed fluid dynamics, control how reactants and products are transported within stagnant and mobile regions in a carbonate rock (Bijeljic et al., 2013), forming different dissolution patterns (Daccord and Lenormand, 1987; Daccord et al., 1993a; 1993b).

Laboratory measurements of batch reaction rates for pure calcite systems in the presence of a reactant are often made using rotating disk experiments (Nierode and Williams, 1971; Plummer et al., 1978; Peng et al., 2015). Such experiments are designed to minimize mass-transport limitations, ensuring that the surface of the sample is always in contact with fresh reactants (Peng et al., 2015; 2016). Compton et al. (1989) concluded that under the influence of a strong acid, calcite dissolution can be modelled as a first-order reaction.

* Corresponding author.

E-mail addresses: r.oliveira16@imperial.ac.uk (R. Oliveira), b.bijeljic@imperial.ac.uk (B. Bijeljic), m.blunt@imperial.ac.uk (M.J. Blunt), acolbourne@slb.com (A. Colbourne), ajs40@cam.ac.uk (A.J. Sederman), mdm20@cam.ac.uk (M.D. Mantle), lfg1@cam.ac.uk (L.F. Gladden).

However, in a porous medium, reactions between an acid and a carbonate rock, such as HCl – CaCO₃ are generally transport-limited. The dissolution patterns are controlled by the combination of the reaction and diffusive characteristic times. Porous media dissolution and the patterns formed have been summarized in terms of transport and reaction times expressed by Damköhler dimensionless numbers by Hoefner and Fogler (1988), Daccord et al. (1989), Daccord et al. (1993a), Fredd and Fogler (1998), Xu et al. (2020). Detwiler et al. (2003) showed how the permeability evolution caused by the dissolution of the surface of fractures is controlled by the advection of reactants. The instability of the dissolution front was later studied by Szymczak and Ladd (2012) by evaluating the growth rate in the reaction and diffusive limits. More recently the results of Menke et al. (2018) and Al-Khulaifi et al. (2018) showed that channel formation and evolution are also strongly influenced by the initial pore structure heterogeneity and flow rate, while Singh et al. (2018) showed how intra-granular porosity can affect the dissolution patterns by increasing the pore connectivity of the sample.

Molecular displacements, or flow propagators, measured by Nuclear Magnetic Resonance (NMR) define the motion of molecules in a given domain (Callaghan, 1993; Seymour and Callaghan, 1997) and are reliable measurements for non-Fickian dispersion in porous media (Scheven et al., 2005b). However the technique can be time-consuming for dynamic systems, so under-sampling methods have been developed to accelerate the acquisitions – such as non-uniform sampling (Scheven et al., 2005a; Mitchell et al., 2008) and compressed sensing (Paulsen et al., 2011). Colbourne et al. (2016) reported an experimental scheme with sufficient time resolution to enable observation of the temporal evolution of the flow propagators during a dissolution experiment. MRI requires longer acquisition times, but can provide a spatially resolved saturation distribution or even fluid saturation profiles (Ramskill et al., 2016). Ramskill et al. (2018) used MRI to monitor the continuous injection of water in a dodecane-saturated Estaiades limestone sample and observed the relative saturations of both phases during a core flood experiment.

There are several modelling techniques that have been successfully employed to study dissolution in porous media. Pore Network Modelling (PNM) is a simple yet powerful method that was introduced by Fatt (1956) and has been widely used to study multiphase flow (Chatzis and Dullien, 1985; Fenwick and Blunt, 1998; Valvatne and Blunt, 2004; Raeini et al., 2018), non-Newtonian fluid flow (Sochi and Blunt, 2008), and porous media dissolution (Raof et al., 2013; Tansey and Balhoff, 2016). The Finite Volume Method (FVM) has been used to study flow, transport and reaction in explicit realizations of the pore space (Meakin and Tartakovsky, 2009; Molins et al., 2012; Liu and Mostaghimi, 2018; Oliveira et al., 2019). Other direct methods include particle-based approaches such as lattice Boltzmann simulation (see, for instance Tian and Wang, 2018) or kinetic cellular automation models (Karapiperis, 1995). Another approach is to couple different methods to overcome particular limitations; for instance Pereira Nunes et al. (2016a,b) coupled the FVM with a Lagrangian particle tracking method to study pore-space dissolution.

The Continuous Time Random Walk (CTRW) concept was proposed by Montroll and Weiss (1965) as a generalization of the Random Walk (RW) method in a regular lattice, where walks would occur to the nearest-neighbouring sites with randomly distributed times. This inspired the development of a generalized transport theory in disordered systems by Scher and Lax (1973a). The method was then used to study impurity conduction in semi-conductors (Scher and Lax, 1973b), followed by the experimental observations and models of Montroll and Scher (1973), Scher and Montroll (1975), Tiedje (1984), Bos and Burland (1987). Later Berkowitz and Scher (1997) and Berkowitz et al. (2000) applied the CTRW formalism to model anomalous transport in random fracture networks and in heterogeneous porous media. The CTRW method was also used to develop an upscaling methodology to integrate pore, core and field scales by em-

ploying different transit-time functions derived from smaller scales by Rhodes et al. (2008). Edery et al. (2010) used CTRW to describe particle transport of a bimolecular reaction system, in which particle of type A reacted with a particle of type B to form a particle of type C, whenever their distance was smaller than an interaction radius. The method was also recently proposed as a tool to model chemical reactions by Ben-Zvi et al. (2018, 2019) by discretising the spatial concentration using the Finite Element Method (FEM) framework. The method is not limited to transport only: for example Aquino and Dentz (2017) used CTRW to derive a generalised chemical master equation that allows general waiting-times between reactions and hence model incomplete mixing in chemical reactions.

In the present work we develop a CTRW transport simulator coupled with a first-order kinetics model to study the dissolution of Kettton carbonate. The principal advantage of this work over the direct simulation methods discussed above is that it uses an upscaled representation of the pore-scale physics, encapsulated in the transition time probability. This enables us to efficiently simulate flow at the cm-scale and match to experiment. We extend the work of Muljadi et al. (2018), that studied the transport signatures of a dissolution experiment using a CTRW framework. Their transport model investigated static snapshots of a Kettton carbonate sample at the beginning and end of a dissolution experiment; here we develop a new reactive transport model to predict the reaction-driven change in porosity and transport properties dynamically with time. We use an NMR dataset to validate our particle transport and reactive flow model. We start by describing the particle transport and reaction model showing the impact of each parameter used. Then we present the available experimental measurements, and build the initial model using the MRI distribution calibrated to the mean porosity and use the distribution of molecular propagators to calibrate the particle mean displacements to the observed propagators. Finally we model the dynamic change in porosity and the evolution of the propagators of the Kettton carbonate sample.

We show that the model is able to qualitatively capture the dissolution channels observed using MRI, and to estimate the effective reaction rate. The model is also able to quantitatively reproduce the distribution of molecular propagators emerging from the dissolution of the sample. Finally we show that by measuring the mean velocity of the particles, we can characterize transport heterogeneity by estimating a value for a transit time power-law scaling coefficient β emerging from the appearance of the dissolved channels.

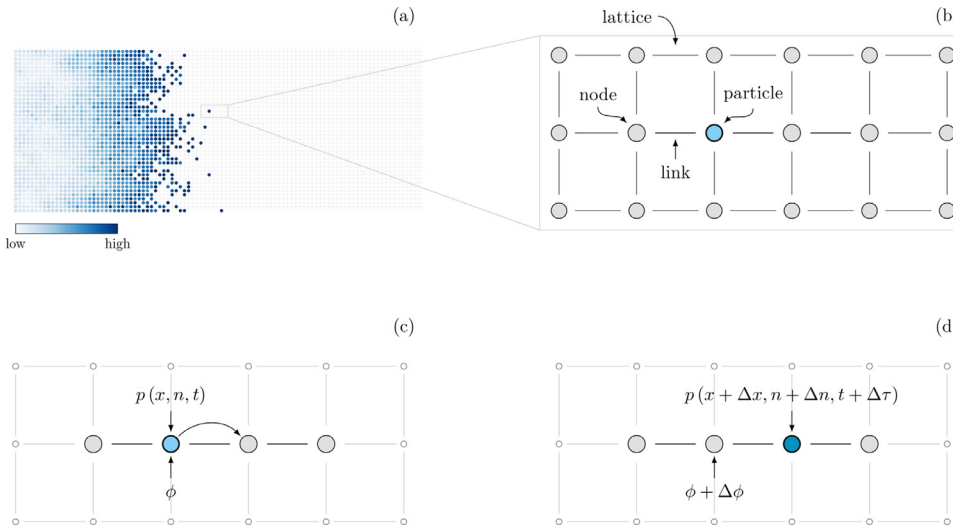
2. Transport and reaction model

Traditional transport models make use of the Advection-Dispersion Equation (ADE) to simulate solute transport in porous media (Bear, 1972) with the inclusion of an additional term to account for reactive processes,

$$\frac{\partial(\phi c)}{\partial t} = -\nabla \cdot (\phi v c) + \nabla \cdot (\phi \mathbf{D} c) + R, \quad (1)$$

where c is the solute concentration, ϕ is the porosity of the domain, v is the Darcy velocity, \mathbf{D} is the dispersion coefficient and R is the reactive term, that either behaves as a sink or a source, according to the process of interest.

Instead of having the solute concentration modelled as a continuous field variable, we describe it using a Lagrangian framework with particles distributed in a lattice (Bijeljic and Blunt, 2006; Le Borgne et al., 2008; Kang et al., 2011; Pereira Nunes et al., 2016a; 2016b). Our modelling approach is conceptually described as follows: a particle contains a number of moles of aqueous calcium. Particles are not created or destroyed; instead the number of moles associated with a particle changes over time. The aqueous calcium concentration is defined as the sum of the moles associated with each particle in a given volume. Solute transport is then modelled as particle transitions in a lattice, carrying the chemical components from site to site. Reactions are then accounted for



as interactions between the chemical components in the particles and the chemical components in the lattice nodes, representing the solid.

Fig. 1 illustrates the transport and reaction of a single particle and shows a given transition step. We describe the state of a particle p in terms of its position x , number of moles of transported species (calcium in this paper) n and time t , or $p(x, n, t)$. The particle transitions are controlled by the particle displacement Δx and transit-time $\Delta \tau$, which are sampled from a Probability Density Function (PDF) that is derived from the pressure and flow field resolved on the lattice. At the end of every transition, the change of aqueous calcium moles associated with a particle Δn and the porosity $\Delta \phi$ in the node of origin is positive due to calcite dissolution at the node during the transit-time.

As the porosity increases, this modifies the underlying pore space, changing the flow field, and leading to the appearance of different dissolution patterns, e.g. channels. Those patterns are likely going to dominate the flow, focusing subsequent particle trajectories in such regions.

Sections 2.1, 2.2 and 2.3 describe the flow, transport and reaction models respectively. **Section 2.4** presents the algorithm detailing the simulation procedure. The model conserves mass both locally and globally, both for the overall mass of aqueous phase and for the calcium tracked as particles through the domain.

2.1. Lattice flow model

The lattice is an abstraction of a grid, with nodes representing the cells and links representing the faces between the cells. This could represent at the pore-scale ($l \approx \times 10^{-6} \text{ m}$) a pore-network, where the nodes and links contain the topological information of pores (wide regions) and throats (restrictions) (Blunt et al., 2013), or at the field-scale ($l \approx \times 10^3 \text{ m}$) it could represent a discretized reservoir model, where the nodes and links represent grid blocks and transmissibility factors (Fanchi, 2006; Rhodes et al., 2009).

The lattice used here represents a 3D porous medium ($l = 4 \times 10^{-3} \text{ m}$, a length where we average over several pores), with each node connected to 6 other neighbouring nodes. Scalar fields are assigned to the nodes and interpolated to the links of the lattice, as illustrated with a simplified 2D domain in **Fig. 2a**.

The scalar fields emerge from a three-dimensional image acquisition where each voxel has defined values of porosity and permeability. Therefore it is only natural to consider the voxel values to be coincident with the values at the nodes of our model requiring us to interpolate them to the links. We calculate the porosity at the link using the arithmetic

Fig. 1. Simplified illustration of an ensemble of particles (a) and the detailed representation of a single particle (b-d) transiting and reacting through a lattice (c-d). The increase of blue depicts an increase of the aqueous calcium concentration. A particle transits in the lattice with variable transit-time $\Delta \tau$ and displacement Δx . After each transition, the number of moles of aqueous calcium in a particle increases by Δn , as a consequence of the reaction within the node of origin, which in turn has its porosity increased by $\Delta \phi$. (For interpretation of the references to color in this figure legend, the reader is referred to the web version of this article)

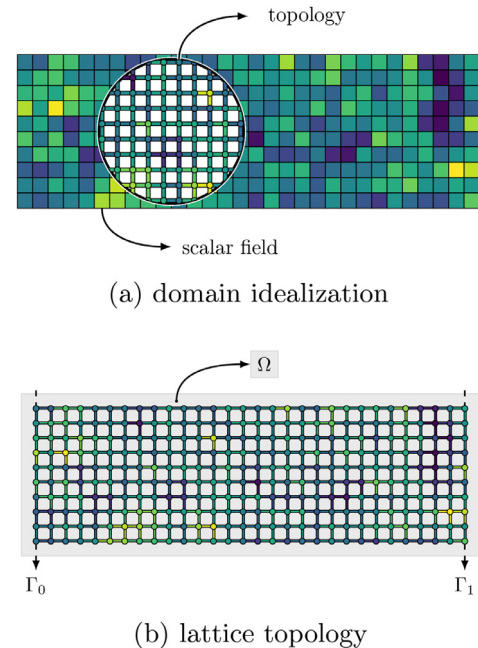


Fig. 2. Domain idealization and lattice topology with scalar fields (porosity and permeability) used to define the nodes and links within the domain Ω and boundaries Γ .

mean of the connected nodes i and j ,

$$\phi_k = \frac{\phi_i + \phi_j}{2}. \quad (2)$$

The permeability K at the link k is calculated using a power-law correlation with the porosity,

$$K_k = a\phi_k^b, \quad (3)$$

where a and b are fitting parameters which can be, as we will show in **Section 4**, based on the experiment. Such power-law correlations between porosity and permeability are widely used, to model the evolution of permeability in dissolution experiments (Menke et al., 2015; Honari et al., 2015).

We solve the pressure field in the lattice for a domain Ω with boundaries Γ , as represented in **Fig. 2b**, by ensuring mass conservation of all

links k leaving node i ,

$$\sum_{\forall k \in i} Q_k = 0, \quad (4)$$

where Q is the volumetric flux at link k , connected by node i and j . The flux $q = Q/A$ is defined within each link k with cross-sectional area A by Darcy's law (Darcy, 1856),

$$q_k = \frac{K_k}{\mu} \frac{P_i - P_j}{l} \quad (5)$$

where K is the permeability at link k , μ the viscosity of the fluid, P the pressure at a node i and l the length of a link (the distance between nodes). At the boundaries Γ of the domain we impose the Dirichlet conditions,

$$P_i = P_{\Gamma_0}, \quad \forall i \in \Gamma_0, \quad (6a)$$

$$P_i = P_{\Gamma_1}, \quad \forall i \in \Gamma_1, \quad (6b)$$

where P_{Γ_0} and P_{Γ_1} are the specified pressures at the boundaries Γ_0 and Γ_1 .

The system of equations formed by Eq. (4) can be written as

$$\mathbf{B}\mathbf{q} = 0, \quad (7)$$

where \mathbf{B} is the network incidence matrix and \mathbf{q} is the flux vector. Then we can define the conductivity matrix for link k between nodes i and j as

$$C_{ij} = \frac{K_k A}{l \mu}, \quad (8)$$

where A is the cross-sectional area and l is its length. Then Eq. (5) can then be written as

$$\mathbf{q} = \mathbf{CB}^T \mathbf{p}. \quad (9)$$

Finally by substituting Eq. (9) in Eq. (7) we obtain the system of equations defining our problem

$$\mathbf{BCB}^T \mathbf{p} = 0. \quad (10)$$

We then solve the linear system of equations in Eq. (10) to obtain the pressure gradient in the links using the Generalized Minimal Residual (GMRES) method (Saad and Schultz, 1986) implemented in the Portable, Extensible Toolkit for Scientific Computation (PETSc) framework (Balay et al., 1997; 2019).

2.2. Particle transport model

We model solute transport as a series of particle transitions in a lattice. The CTRW joint probability distribution $\psi(\mathbf{x}, t)$ can be described in terms of a decoupled probabilities of spatial displacement $p(\mathbf{x})$ and transition time $\psi(t)$, $\psi(\mathbf{x}, t) = p(\mathbf{x})\psi(t)$. The particle transitions are then governed by the decoupled probability distributions for the transition time and displacement of the particles. This concept is explored in Dentz et al. (2004) and Berkowitz et al. (2006). Fig. 3 shows an idealization of the lattice with a node i at the origin connected to nodes $j \in 0, 1, \dots, N$ through a link k . Each link has a calculated probability of displacement p_{ij} and probability of transit-time ψ_{ij} (Fig. 3b) using the underlying properties of the link.

The transit-time distribution ψ_{ij} is represented by a Truncated Power-Law (TPL) distribution which empirically, matches experimental results (Levy and Berkowitz, 2003) defined using two different characteristic time scales (Dentz et al., 2004; Bijeljic and Blunt, 2006) and an adjustable parameter

$$\psi(t) = Ae^{-t/t_1}(1+t/t_1)^{-1-\beta}, \quad (11)$$

where t_1 is the advective transit time, t_2 is the diffusive cut-off time, β is a fitting parameter representing the heterogeneity of the medium and A is a normalization constant such that $\int_0^\infty \psi(t')dt' = 1$ meaning that ψ can be used as a PDF.

The probability for a transition to occur in the interval $(t, t + dt]$ is $\psi(t)dt$ and the parameters in Eq. (11) are defined as

$$t_1 = \frac{l}{|v_{ij}|}, \quad (12a)$$

$$t_2 = \frac{l^2}{D_m}, \quad (12b)$$

where v_{ij} is the velocity in the link between nodes i and j , D_m is the molecular diffusion coefficient and l is the length of the link. In this work we assume that l and D_m are fixed; however, because the velocity in each link is different, the transit time distribution will also vary from link to link.

Eq. (11) is empirical yet successfully reproduces non-Fickian transport signatures at different time scales (Dentz et al., 2004; Berkowitz et al., 2006; Bijeljic and Blunt, 2006; Berkowitz and Scher, 2009; Edery et al., 2015). We do not fit the values of t_1 and t_2 in Eq. (12); these are directly calculated from the flow field and the transport parameters. The velocity used to calculate t_1 is $v_k = v_{ij}$, the velocity in the link k between nodes i and j . The value of β however is fitted to experimental measurements. The asymptotic analysis for the mean velocity v of a plume of solute in Dentz et al. (2004) showed that for values of $\beta < 1$, $v \propto t^{\beta-1}$ and for $1 < \beta < 2$, v is constant.

Lastly the probability of transition from node i to node j is calculated from the asymptotic solution of the ADE. The solution is developed in Rhodes and Blunt (2006) and generalized in Rhodes et al. (2008) as

$$p_{ij} = G \frac{Pe_{ij}}{1 - e^{-Pe_{ij}}}, \quad \forall v_{ij} > 0 \quad (13a)$$

$$p_{ij} = G \frac{Pe_{ij}}{e^{Pe_{ij}} - 1}, \quad \forall v_{ij} < 0 \quad (13b)$$

where Pe is the Péclet number, $Pe_{ij} = l|v_{ij}|/D_m$ is the locally defined Péclet number in the link connecting node i to node j , and G is a normalization factor such that $\sum_j p_{ij} = 1$. Simplifications of Eq. (13) are very important when implementing the numerical model and are detailed in Appendix A.

2.3. Calcite dissolution model

The main assumption in our reaction model is that dissolution is modelled with first-order kinetics in an ideal solution. We also do not allow the fluid to become over-saturated, so we do not allow precipitation. Finally, we will assume a constant specific surface area for reaction which does not change over time.

As mentioned in Section 2.1, we discretize our domain as a lattice with properties defined in both nodes and links. This lattice represents a Kettton limestone, which is nearly entirely composed of calcite (Andrew et al., 2014). Thus we define the number of moles of calcium in each node which is equal to the number of moles of calcite:

$$n_{i,Ca^{2+}} = n_{i,CaCO_3} = (1 - \phi_i)V \frac{\rho_{CaCO_3}}{M_{CaCO_3}}, \quad (14)$$

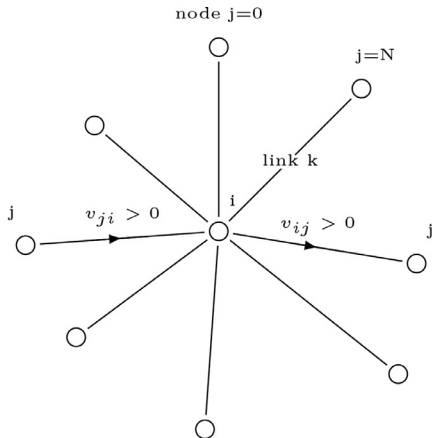
where $V = l^3$ is the effective volume of the node, ϕ_i the porosity of the node, ρ the density of calcite (2.71×10^3 kg/m³) and M the molar mass of calcite (0.1kg/mol).

Dissolution occurs as particles containing acid, or H⁺ rich particles, are injected in the domain and are allowed to react with the calcite rich nodes in the lattice.

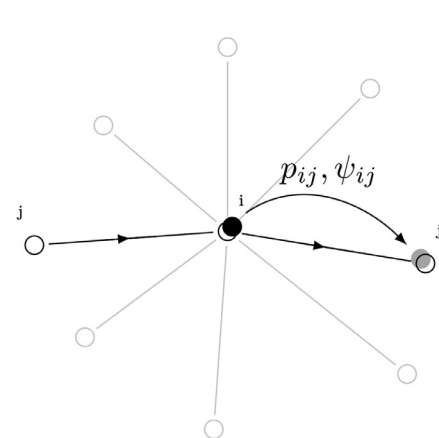
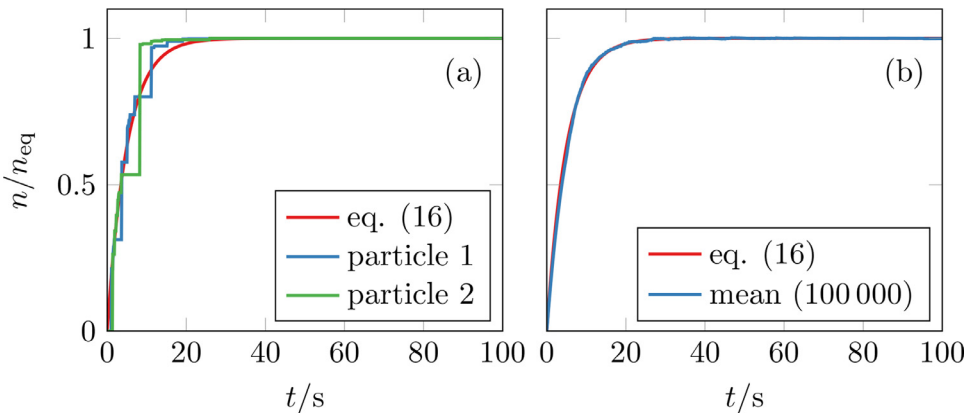
This releases calcium from solid (in calcium carbonate) to the aqueous phase. We track the amount of calcium in the aqueous phase, following the approach of Pereira Nunes et al. (2016a,b).

Dissolution is assumed to be first-order with the concentration of H⁺, so that it is described with a first-order kinetic model where the number of moles of Ca²⁺ in a particle $n_{Ca^{2+}}$, or simply n , is

$$\frac{dn}{dt} = k_r(n_{eq} - n), \quad (15)$$



(a) General lattice consisting of an arbitrary number of nodes and links

(b) Particle transition from node i to node j with probability p_{ij} and ψ_{ij} 

where n_{eq} is the number of moles in a particle in equilibrium and $n_{eq} - n$ represents the departure from equilibrium. Eq. (15) can be solved analytically such that

$$n = n_{eq}(1 - e^{-k_r t}). \quad (16)$$

The increase in moles of calcium associated with a particle is calculated in the node of origin at the end of each transition. The change of moles of aqueous calcium, Δn , is assumed to be proportional to the particle transit-time, such that Eq. (15) is approximated to:

$$\frac{dn}{dt} \approx \frac{\Delta n}{\Delta \tau} = k_r(n_{eq} - n), \quad (17)$$

with the particle transit-time chosen from the distribution defined in Eq. (11).

To illustrate this process, Fig. 4 shows the evolution of moles of Ca^{2+} for two different particles and the mean evolution for an ensemble of 100000 particles as they transit and react in a homogeneous system. This system is represented by constant characteristic times $t_1 = 0.03 \text{ s}$, $t_2 = 3.0 \text{ s}$ and $\beta = 1.6$, and the reaction rate constant is $k_r = 0.2 \text{ s}^{-1}$. The Ca^{2+} evolution is compared against the analytical solution in Eq. (16).

The increase of moles of dissolved calcium in the particle incurs a decrease of moles of calcite in the lattice nodes, such that after a transit-time $\Delta \tau$, the particle increases its moles by Δn and the node from which the particle originated its transition loses the same number of moles. As we assume that the solid domain is composed entirely of calcite, removing calcite from a node proportionally increases the porosity. We relate the increase of porosity ϕ_i with the amount of calcite n_i in the node after a particle transition,

$$\Delta \phi_i = \phi_i^{t+\Delta \tau} - \phi_i^t, \quad (18a)$$

Fig. 3. General lattice consisting of nodes interconnected by links. This depicts a particle transition from a node i to a node j through a link k with prescribed velocity v , probability of displacement p_{ij} and transit time distribution ψ_{ij} .

Fig. 4. Comparison between the analytical solution of the moles of aqueous calcium defined in Eq. (16) and the simulated results using Eq. (17) and Eq. (11) for (a) two particles and for (b) the mean of 100000 particles. The model uses $k_r = 0.2 \text{ s}^{-1}$, $t_1 = 0.03 \text{ s}$, $t_2 = 3.0 \text{ s}$ and $\beta = 1.6$. The change in the number of moles of aqueous calcium associated with each particle is proportional to the particle transit-time at the end of each transition.

$$\Delta n_i = n_i^{t+\Delta \tau} - n_i^t = k_r \Delta \tau (n_{eq} - n_i^t). \quad (18b)$$

From Eq. (18a) and Eq. (14) we relate the change of porosity ϕ_i with the change of calcite moles in the node and to the corresponding change in Ca^{2+} moles in the particle as

$$\Delta \phi_i = \Delta n_i \frac{M_{\text{CaCO}_3}}{V_i \rho_{\text{CaCO}_3}}. \quad (19)$$

To estimate the reaction rate constant k_r of the particles in a node, we relate it to the surface reaction rate r measured in laboratory experiments as

$$k_r = \frac{V \sigma_A}{n_{eq}} r, \quad (20)$$

where σ_A is the specific surface area of the node, which we assume is constant throughout the domain, and during the dissolution processes. This is a strong assumption, but, as we show later, allows accurate predictions to be made. The batch reaction rate, r , was measured by Peng et al. (2015) to be $1.5 \times 10^{-3} \text{ mol m}^{-2} \text{ s}^{-1}$ and is used to estimate $k_r = 6.28 \times 10^{-1} \text{ s}$ where the other parameters used are given in Table 1.

2.4. Reactive transport algorithm

The algorithm describing the transport and reactive model consists of three solvers:

1. **Flow solver** – calculates the pressure gradient, and hence the local velocities, the initial transit-time and displacement probability functions (defined in Section 2.1).

Table 1
Model properties and dissolution parameters.

Parameter	Symbol	Value	SI Units
Total simulation time	t_{\max}	1.25×10^4	s
Volumetric flux	Q	5.3×10^{-7}	$\text{m}^3 \text{s}^{-1}$
Mean velocity	v	3.06×10^{-3}	m s^{-1}
Molecular diffusion coefficient of Ca^{2+}	$D_{m,\text{Ca}^{2+}}$	1.15×10^{-9}	$\text{m}^2 \text{s}^{-1}$
Molecular diffusion coefficient of H^+	D_{m,H^+}	1.92×10^{-9}	$\text{m}^2 \text{s}^{-1}$
Heterogeneity parameter	β	0.9	
Specific surf. area (Menke et al., 2015)	σ_A	8.0×10^3	m^{-1}
Batch reaction rate (Peng et al., 2015)	r_{calcite}	1.5×10^{-3}	$\text{mol m}^{-2} \text{s}^{-1}$
Reaction rate constant	k_r	6.28×10^{-1}	s^{-1}
Number of moles at equilibrium	n_{eq}	8.3×10^{-10}	mol
Longitudinal model size	L_x	7.2×10^{-2}	m
Transversal model size	$L_{y,z}$	2.7×10^{-2}	m
Length of links	l	4.0×10^{-4}	m
Total number of links	N_{links}	1.89×10^6	
Total number of nodes	N_{nodes}	6.48×10^5	
Number of injected particles per Δt	$N_{\text{particles}}$	1.0×10^3	

2. **Transport solver** – solves for the individual particle transitions within a time step (defined in Section 2.2).
3. **Reactive solver** – calculates the calcite dissolution and porosity alterations proportional to the particle transit-time (defined in Section 2.3).

Each particle transits independently of one another; we require that after a number of transitions, we synchronize all particles at a common checkpoint with a time-step Δt . The synchronization is needed to have the particles stationary at a particular time so that the pressure field can be re-calculated by the flow solver while the time and displacement probabilities are updated. Particles are continuously injected in the domain, but for practical reasons and in order to conserve reactant influx in the model, we do it at every Δt checkpoint. The particles are only considered valid and kept in the simulation while $|n - n_{\text{eq}}| > \epsilon$, with ϵ being the computer's floating point precision. The particles are also removed from the simulation if they reach the exit boundary, $x > L_x$, such that no back-diffusion is allowed at the outflow. This is to ensure the computational efficiency of the simulation.

The steps in the algorithm are listed below:

1. Create the lattice with an initial distribution of porosity ϕ and permeability K .
2. Solve the pressure field P in the lattice, calculate the local velocities v_{ij} and local Péclet numbers Pe_{ij} in the links.
3. Calculate the local probabilities of displacement p_{ij} Eq. (13) and the local transit-time distribution ψ_{ij} Eq. (11) in the links.
4. Inject the particles in the inlet using a flow-weighted injection rule.
5. Sample a displacement direction Δx from p_{ij} and transit-time $\Delta\tau$ from ψ_{ij} for each particle.
6. Move the particle from the node i to the node j , if $\sum \Delta\tau^m \leq \Delta t$, where m labels each particle transition. This is performed individually for each particle.
7. Increase the moles of aqueous calcium in the particle moles by Δn Eq. (18b) using the sampled transit-time $\Delta\tau$.
8. Dissolve the solids in the node of origin i and increase the porosity by $\Delta\phi$, Eq. (19).
9. Repeat steps 5–8 for all particles while $\sum \Delta\tau^m \leq \Delta t$. Each particle can undergo several transitions in one time step before the pressure field is updated.
10. Update the pressure field P if the mean porosity change is higher than a given threshold.
11. Repeat steps 2–10 until the end of the simulation.

The pressure field needs to be updated after the particles have changed the porosity in the nodes. At the end of each time step Δt , we calculate the domain mean porosity difference $\Delta\phi$ and if it is smaller than a given precision ϵ_ϕ we continue, otherwise the pressure field is

Table 2
Ketton carbonate sample properties and dissolution experimental parameters.

Parameter	Symbol	Value	SI Units
Volume injected	Vol_{HCl}	1.0×10^{-2}	m^3
Concentration	c_{HCl}	1.0×10^{-2}	mol L^{-1}
Total time	t_{\max}	1.25×10^4	s
Volumetric flux	Q	8.3×10^{-7}	$\text{m}^3 \text{s}^{-1}$
Mean velocity	v	3.06×10^{-3}	m s^{-1}
Mean initial porosity	$\bar{\phi}_0$	0.24	
Molecular diffusion coefficient	D_m	1.92×10^{-9}	$\text{m}^2 \text{s}^{-1}$
Sample length	L	7.2×10^{-2}	m
Sample radius	R	1.9×10^{-2}	m
Péclet number	Pe	5.9×10^2	
Damköhler number	Da	7.7×10^{-5}	

re-calculated. The present study found that $\epsilon_\phi = 1 \times 10^{-4}$ was sufficient to keep the results consistent, in that more frequent recomputations of the flow field did not affect the results, as shown later in Section 4.3.

3. NMR experiments

Ketton limestone dissolution was characterized using NMR propagators and imaging techniques. Molecular propagators and 1D porosity profiles were continually acquired during the whole duration of the experiment, and a 3D porosity map was acquired at the beginning and at the end of the experiment. This data was used to calibrate the modelling method proposed in this study. All NMR measurements were done using a Bruker BioSpin AV spectrometer with a 2 T horizontal bore superconducting magnet (85 MHz ^1H frequency) and a 60 mm diameter birdcage radiofrequency (RF) coil.

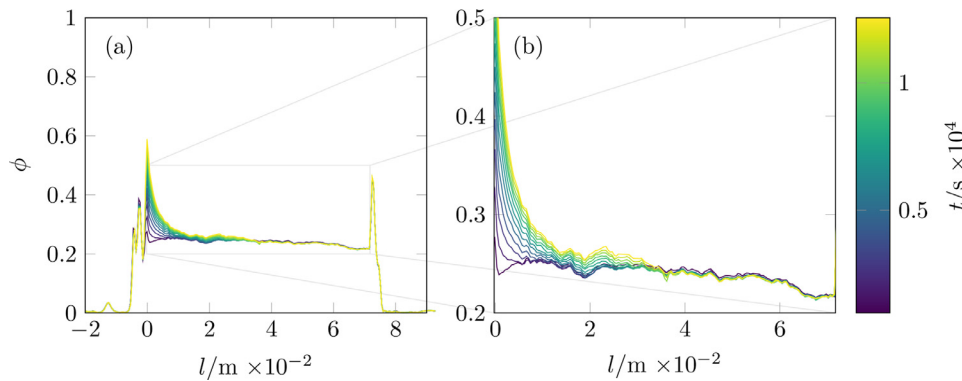
The cylindrical Ketton sample had a length and diameter of 0.072 m and 0.038 m respectively, and was mainly composed of calcite (Andrew et al., 2014).

The whole experiment lasted for approximately 3.5 h and a total of 10 L of 0.01 mol L^{-1} HCl was injected through the sample: initially the sample was fully-saturated with distilled water under vacuum. The residence time of the fluid in the transfer lines from the pump to the sample were minimal compared to the experiment duration and therefore initial dilution when the acid was first pumped was insignificant. The measured flow rate was $8.3 \times 10^{-7} \text{ m}^3 \text{s}^{-1}$, with a superficial velocity of $3.06 \times 10^{-3} \text{ m s}^{-1}$.

The global Péclet number is defined as $\text{Pe} = L/v/D_m = 5.9 \times 10^2$ and the global Damköhler number is defined in Menke et al. (2016) as $\text{Da} = \pi r/\langle v \rangle n = 7.7 \times 10^{-5}$. Table 2 contains a summary of the experimental parameters.

1D porosity profiles were acquired with a spin echo sequence with readout gradient. The measurements were optimised for minimum echo-time to minimise relaxation and motion weighting of the overall signal in order to produce quantitative local porosity measurements. 256 complex data points were acquired with a spectral bandwidth of 400 kHz and an echo time of 0.96 ms. The field-of-view (FOV) was set to 112.8 mm giving a spatial resolution of the local porosity of 0.44 mm. Gravimetric measurements of average porosity were made for individual cores and the signal amplitude of the profiles scaled accordingly to provide quantitative porosity measurements. 3D images, using the RARE (Hennig et al., 1986) acquisition method, were acquired with $256 \times 128 \times 128$ voxels and an isotropic resolution of $391 \mu\text{m}$; a recycle time of 1.5 s, echo time of 2.8 mm, and RARE-factor of 32 giving a total image time of 43 min 47 s. For both 1D and 3D images, hard pulses were used for both the 90° and 180° pulses and trapezoidal gradients were used to minimise the echo-time.

The probability distribution of molecular displacements $P(\zeta)$, also known as a propagator, is obtained by observing water molecule displacements ζ during a given observation time Δ . Molecular propagator distributions are often normalized by the mean displacement ζ_0 , in-



dicating the transport heterogeneity when the distribution is far from $\zeta/\zeta_0 = 1$ and have asymmetrical shape (Scheven et al., 2005a). Under-sampled and spatially resolved propagator measurements were used to monitor the change in the distribution of fluid displacement as a function of position along the flow direction. Spatially Resolved Propagator (SRPs) were acquired using a modified alternating gradient pulse stimulated echo (AGPSTE) sequence (Cotts et al., 1989), where the acquisition is done in the presence of a readout gradient to obtain a spatially (X) resolved acquisition. The undersampling and reconstruction of the propagator was performed as previously described (Colbourne et al., 2016), with the individual reconstruction of q -space for each point in k-space. The spatially resolved dimension was acquired with the same parameters as the 1D profile experiments described above. The displacement encoding acquisition parameters were as follows: observation time, $\Delta = 250$ ms; number of acquired q -space points, 41; gradient pulse duration, $\delta = 2.5$ ms; and maximum applied magnetic field gradient strength, $g_{\max} = 10.5$ Gcm⁻¹. The flow gradient was aligned with the superficial flow direction.

The 1D profiles and SRPs were acquired at 966 s intervals throughout the dissolution experiment whereas the 3D images were acquired before dissolution had started and at the end of the dissolution experiment after 10 L had flowed through the rock core.

4. Results

We start with presenting the NMR experimental results from Ketton limestone dissolution in Section 4.1, detailing the evolution of the 1D porosity profiles, the 3D porosity images and finally the SRPs. Furthermore, we show the Ketton limestone model in Section 4.2 and then in Section 4.3 we describe the calcite dissolution model, detailing the results for the evolution of porosity, dissolution rate and particle propagators and comparing it with the experiment.

4.1. NMR experimental results

4.1.1. 1D porosity profiles

The 1D porosity profiles were obtained at fixed intervals of 966 s, capturing not only the sample but the rock core holder entry and end effects, as illustrated in Fig. 5. The sample is located between the origin and approximately 0.072 m. The profiles show that the highest porosity alteration is in the first 0.015 m of the sample, then is sharply reduced, remaining nearly constant in the 0.035 m to 0.055 m interval, while the alteration in porosity is almost negligible near the outlet. The fluctuations in porosity reflect the natural heterogeneity of the rock.

This behaviour is better illustrated in Fig. 6, where we display the relative difference in the porosity as the dissolution experiment progresses; the change in porosity is limited to the first 0.05 m from the inlet.

4.1.2. MRI acquisition

The 3D magnetic resonance porosity measurements of the sample was only acquired at the beginning and end of the experiment. The total

Fig. 5. (a) Porosity profile evolution from the beginning to the end of the dissolution experiment. (b) The region where the sample is located is highlighted from approximately 0m to 0.072 m. The porosity profiles are coloured accordingly to the acquisition time, from the beginning of the experiment to the end at 1.254×10^4 s. The highest porosity alteration can be seen in the first 0.015 m of the sample, reducing sharply and is nearly absent after 0.055 m.

size of the image is 256 voxels in length, by 128 and 128 voxels in width and height, with the Region of Interest (ROI) defined by a cylinder with radius of 57 voxels and length of 180 voxels.

The 3D MRI porosity was normalized to match the 1D MRI porosity profiles, for consistency. Fig. 7 shows the normalized MRI image at the beginning and end of the experiment. The flow channels formed are highlighted in the second image by applying an opacity filter for $\phi < 0.3$.

4.1.3. NMR propagator measurements

Fig. 8 shows the propagators at the entry and exit of the sample during the whole duration of the dissolution experiment, and the difference between the first and last acquisitions. The entry of the sample underwent the most significant alterations, while the exit of the sample was left nearly intact which is consistent with the negligible change in porosity, consistent with the results shown in Fig. 5. The complete description, with acquisitions at every 0.005 m of the sample, is displayed in Fig. B.1 in Appendix B.

4.2. Ketton carbonate model

The model for the Ketton carbonate sample dissolution described in the previous section, is divided into three main steps:

1. Creation of the initial porosity and permeability model;
2. Calibration of β using the experimentally measured propagators;
3. Development of the dissolution simulation.

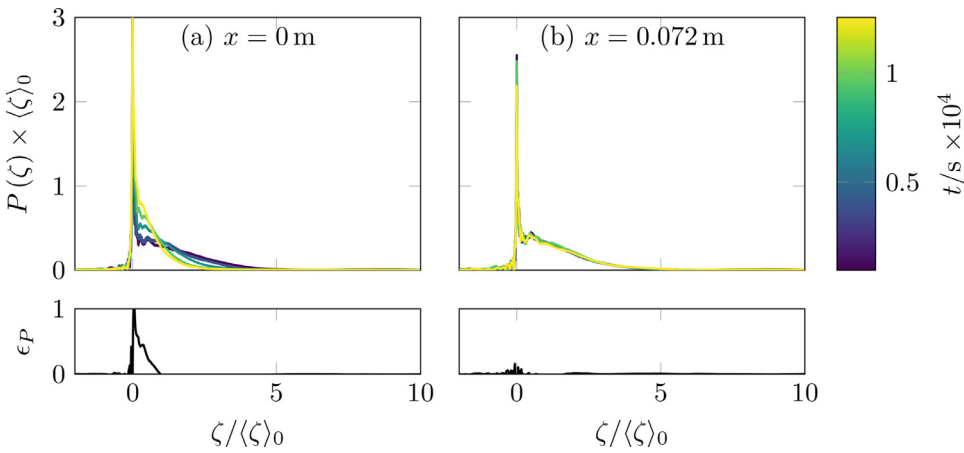
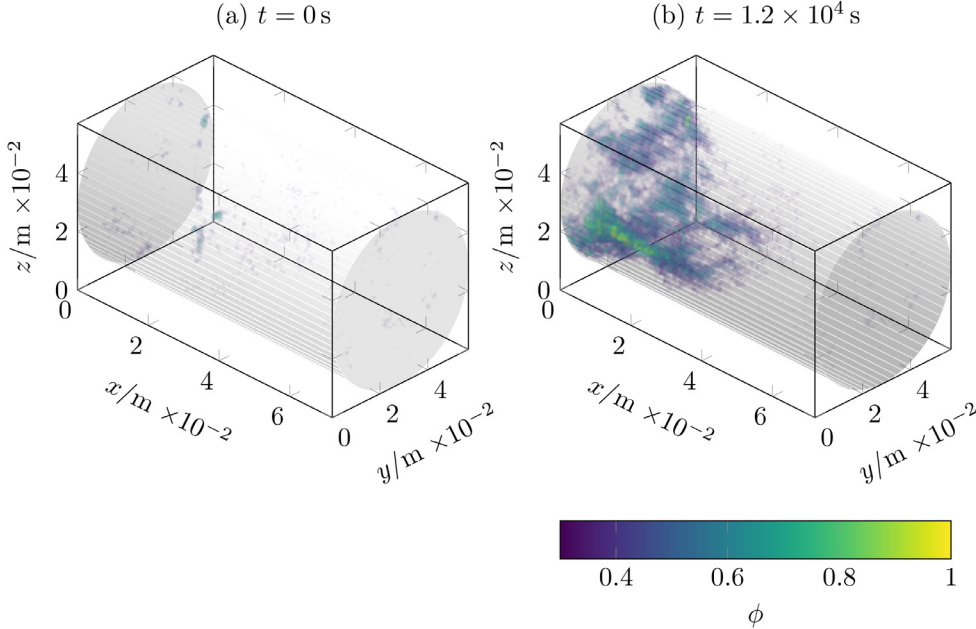
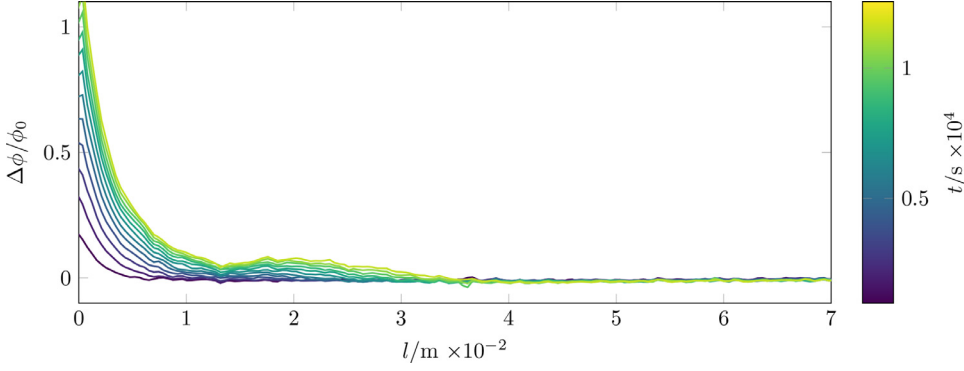
The initial static model is calibrated using experimental data to ensure an approximation of the initial state of the sample. The results from the dissolution simulation, such as the porosity during dissolution and particle propagators, are then compared to the experimental measurements.

4.2.1. Initial model calibration

Our model is three-dimensional and the initial porosity ϕ_0 is constructed using the 3D MRI-derived porosity, described in the previous section. The initial permeability K_0 is then calculated using the power-law correlation of the porosity in Eq. (3). The coefficients in the correlation are based on the Ketton permeability measurements of Honari et al. (2015) with $a = 2.2 \times 10^{-8}$ m² and $b = 6.2$, and the resulting distributions are presented in Fig. 9.

With the initial porosity and permeability distributions, we solve the pressure distribution by imposing a gradient of $\Delta P = 1$ Pa, and then scale the resulting velocity field to obtain the correct mean velocity of the experiment $\langle v \rangle = 3.06 \times 10^{-3}$ ms⁻¹. The initial porosity field and the calculated pressure are displayed in Fig. 10. The porosity distribution shows a heterogeneous sample, which directly reflects the MRI experimental data used to build the model.

Having defined the initial porosity, permeability and flow field of the model, we can calculate the local ψ functions in each link. Our main assumption is that the characteristic times t_1 and t_2 of the ψ functions are



defined from the flow field and transport parameters while the β parameter is set the same for all links. β accounts for pore-scale heterogeneity in the transport, below the scale of the underlying lattice, l : the effective value of β is related to the assumed lattice size l . We fix l and find β that provides an accurate representation of transport before dissolution. We will assume that β remains constant in both space and time during the dissolution process. The value of t_1 is calculated from the flow velocity in each link using Eq. (5). The value of t_2 is calculated from

the molecular diffusion coefficient at 18°C, $D_{m\text{H}_2\text{O}} = 1.92 \times 10^{-9} \text{ m}^2\text{s}^{-1}$ (interpolated from the values in the [Bruker Almanac, 2013](#)) for the simulation of the propagators.

We find β by evaluating the particle propagators from the simulation and fitting them to the experimentally-measured propagators. This is obtained by injecting a pulse of particles, observing the particles for $\Delta = 0.25$ s and measuring the difference between the experimental and modelled distribution of displacements. We analyse the resulting par-

Fig. 6. Evolution of porosity difference from the beginning to the end of the dissolution experiment. The region where the sample is located between 0.00 m and 0.072 m. The porosity profiles are coloured accordingly to the acquisition time, from the beginning of the experiment to the end at 1.254×10^4 s.

Fig. 7. Porosity field for the carbonate sample at the beginning (a) and at the end (b) of the dissolution experiment. The porosity is normalized using the 1D porosity profiles. The channel formed is visualised in the second image by applying an opacity filter for $\phi < 0.3$.

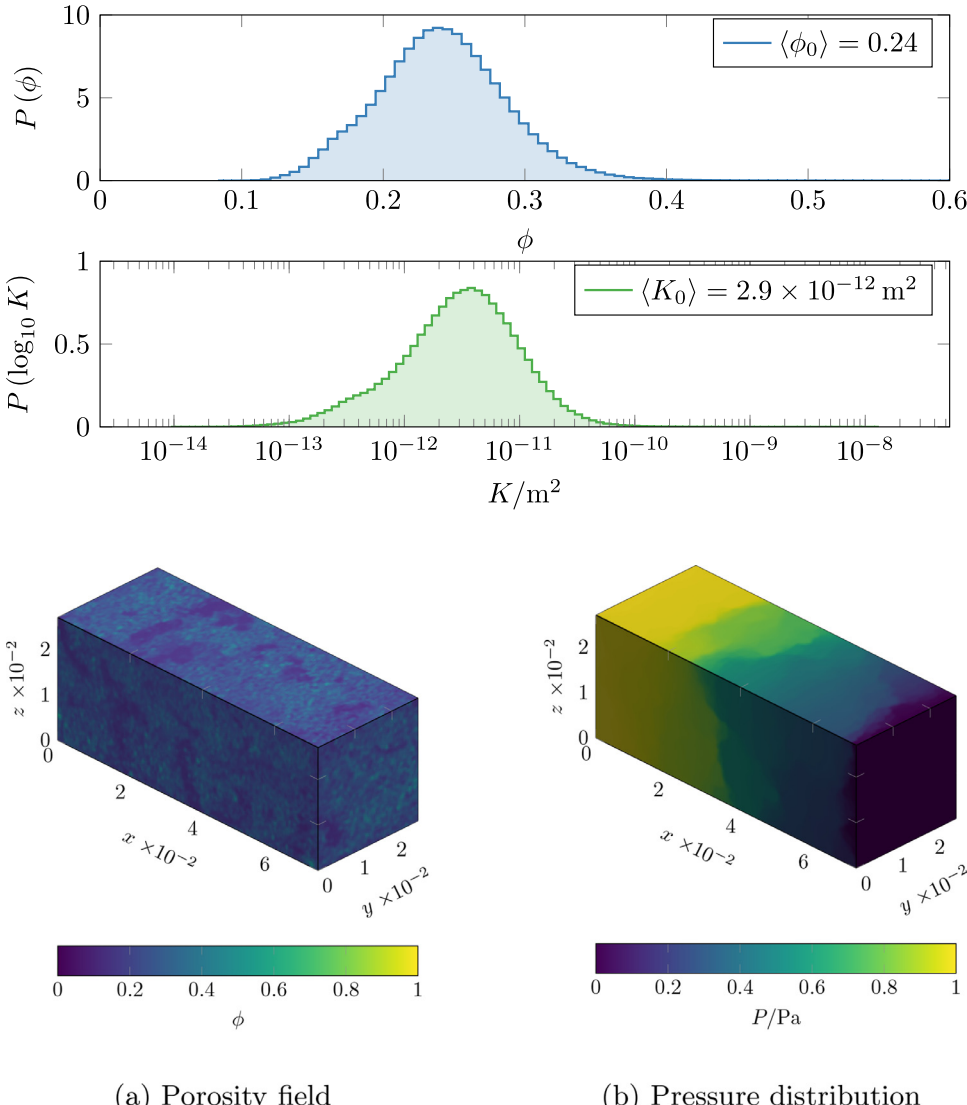


Fig. 9. Initial porosity and permeability distribution. The porosity-permeability correlation factors $a = 2.2 \times 10^{-8} \text{ m}^2$ and $b = 6.2$ are defined in Eq. (3) and based on the Ketton limestone experiments by Honari et al. (2015).

Fig. 10. Initial porosity field and calculated pressure. The porosity is constructed from the MRI acquisition. The calculated pressure reflects the initial heterogeneity of the sample modelled after the MRI-derived porosity.

Table 3

Parameters used and the KS-test between the particle propagators and the experimental propagators for different fitted values of β . The value of $\beta = 0.9$ scored the highest KS-test and was selected for subsequent simulations.

Parameter	Symbol	Value	SI Units
Mean velocity	$\langle v \rangle$	3.06e-3	m s^{-1}
Molecular diffusion coefficient of H_2O	D_m	1.92e-9	$\text{m}^2 \text{s}^{-1}$
Advection transit time	t_1	0.0261	s
Diffusive cut-off time	t_2	8.50	s
Transport heterogeneity parameter	β	KS-test	
	0.5	0.0534	
	0.7	0.0589	
	0.9*	0.2237	
	1.1	0.0647	
	1.3	0.0103	
	1.5	0.0045	

[*] selected value.

particle propagator distribution from the simulation with the measured molecular propagator distribution and show the results in Table 3. To compare the results, each model case was compared against the experimental distribution using the Kolmogorov-Smirnov (KS) test, for

which the higher the p -value, the more similar are the distributions (Kolmogorov, 1933; Smirnov, 1939). The particle propagator distribution for the highest KS-test value of 0.22 is shown in Fig. 11. Lower values of β overestimate the number of slower particles ($\zeta/\langle\zeta\rangle_0 < 1$) and underestimate faster particles ($\zeta/\langle\zeta\rangle_0 > 1$). The value of $\beta = 0.9$ was selected for the simulations and used in the dissolution models presented next.

4.3. Calcite dissolution modelling

HCl with a molar concentration of 0.01 mol L^{-1} is injected at a rate of $Q = 8.3 \times 10^{-7} \text{ m}^3 \text{s}^{-1}$, see Table 2, equivalent to injection of H^+ at $8.3 \times 10^{-6} \text{ moles s}^{-1}$. The value of t_2 is calculated from the molecular diffusion coefficient at 18°C $D_m \text{Ca}^{2+} = 1.15 \times 10^{-9} \text{ m}^2 \text{s}^{-2}$ (extrapolated from the values in Ribeiro et al., 2008) to account for the aqueous calcium in the particles. We choose the value of $N_{\text{particles}} = 1000$ for a time step $\Delta t = 10 \text{ s}$; injecting more particles had no effect on the results. Fig. 12 shows the porosity profiles after $1 \times 10^3 \text{ s}$ for different numbers of injected particles, 10^2 and 10^3 . Injecting 10^4 particles gave no additional difference and was omitted from the plot. The model is built using the parameters summarised in Table 1.

The pressure field is recalculated whenever the total porosity increment $\Delta\phi > 1 \times 10^{-4}$. Reducing this value increases the amount of times

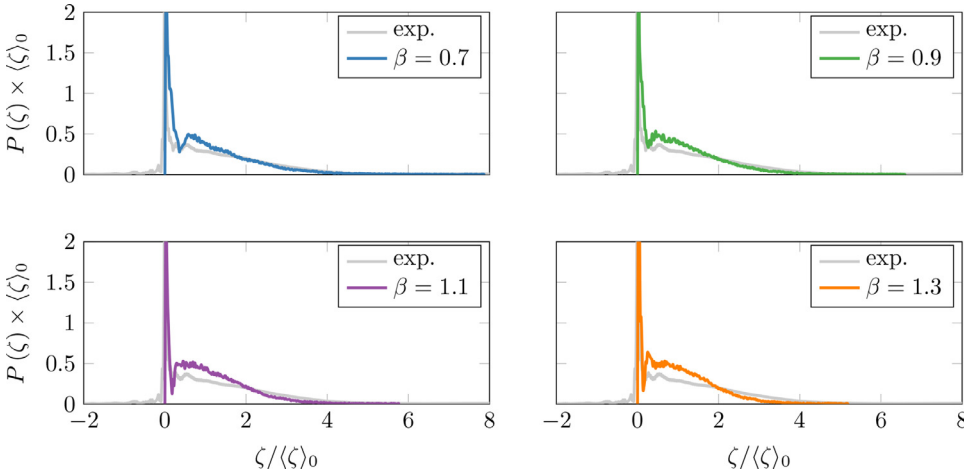


Fig. 11. Particle propagator distribution for different values of β . The best fit was obtained with $\beta = 0.9$.

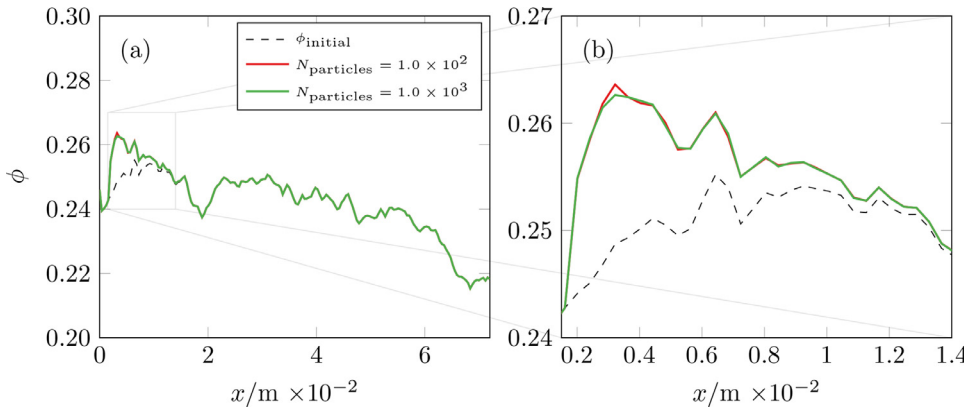


Fig. 12. Porosity profiles (a) and zoomed-in detail (b) along the flow direction for different numbers of injected particles per time step, at the beginning and at $t = 1 \times 10^3$ s. We used $N_{\text{particles}} = 1000$ for a time step $\Delta t = 10$ s as the optimum number of particles injected by observing that the porosity profile did not change if more particles were injected.

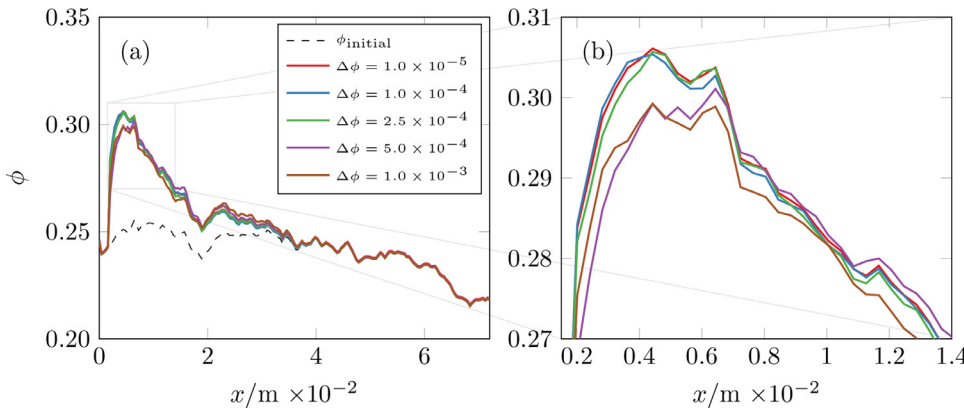


Fig. 13. Porosity profiles (a) and zoomed-in detail (b) along the flow direction for different porosity change precisions at the end of the simulation. We choose the value of $\Delta\phi = 1 \times 10^{-4}$ as the optimum total porosity change to update the pressure field. Reducing this value increases the amount of times that the pressure is updated, but showed no influence in the porosity evolution.

that the pressure is updated, but this had no influence on the predicted changes in porosity. Fig. 13 shows the porosity profiles for different porosity increments, illustrating this point. The selected time step is $\Delta t = 10.0$ s and the other parameters used in these cases are the same as shown before in Table 1.

4.3.1. Porosity evolution

The evolution of porosity obtained in the model is compared against the experimentally measured porosity profiles in Fig. 14, the dissolution channels formed are shown in Fig. 15, and the geometries of the channels are described in Table 4 from manual analysis of the images. The first 0.002 m of the model is omitted as it is used as buffer layer to homogenize the flow at the inlet. The simulation reflects the experimental behaviour of the NMR porosity profiles, where most of the dissolution

Table 4

Comparison between the geometries of the experimental acquisition and simulated model for the channel formed by dissolution.

Parameter	Symbol	Exp.	Sim.
Centre coordinate /m	y_c	2.35e-3	2.62e-3
	z_c	6.06e-3	4.67e-3
Total length /m	l_c	2.88e-2	2.52e-2
Mean radius /m	r_c	1.90e-3	1.28e-3

happens at the entry of the sample and is nearly absent after. There is a small discrepancy near the inlet with an under-prediction of the poros-

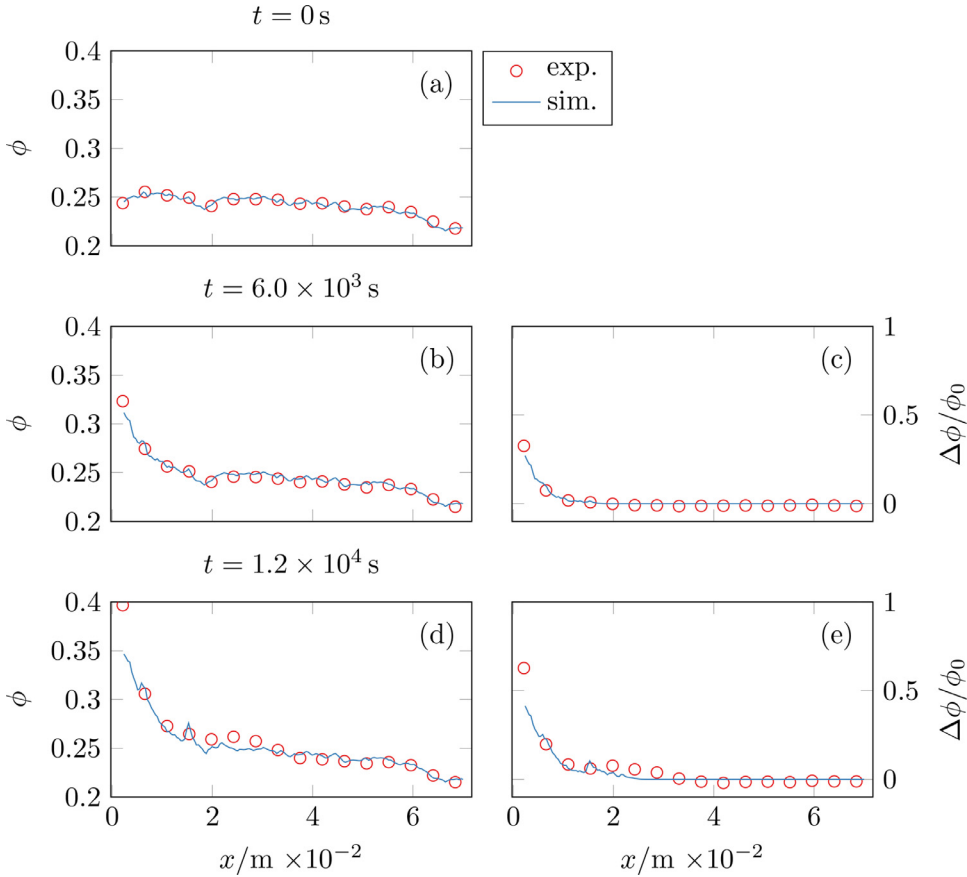


Fig. 14. Profiles for the simulated porosity and relative porosity difference compared to the experimentally-measured NMR porosity profiles. Figure (a) shows the initial porosity profile, figure (b) and (c) the porosity and porosity difference at $t = 6.0 \times 10^3$ s, and figure (d) and (e) at the end of the experiment, $t = 1.254 \times 10^4$ s.

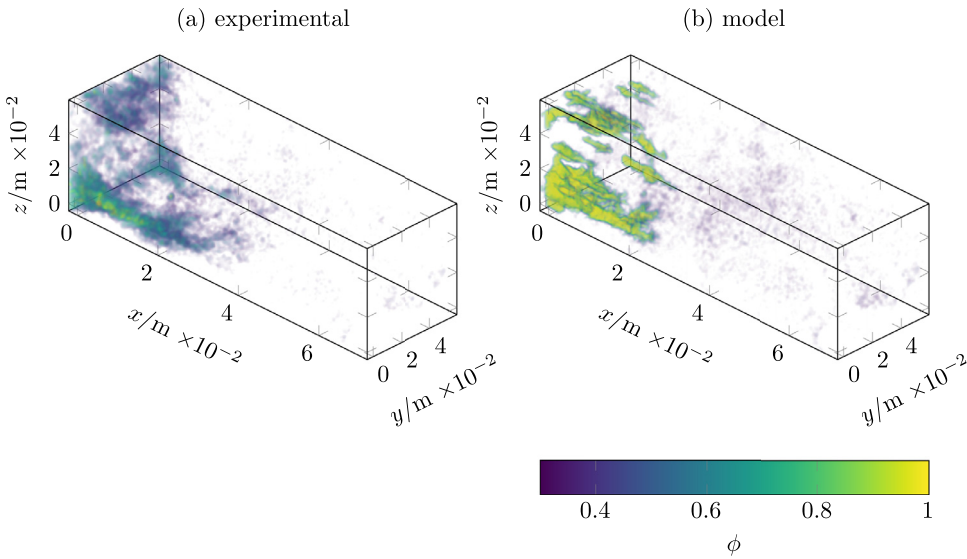


Fig. 15. Porosity field in the experiment (a) and simulation (b) at 1.254×10^4 s, at the end of the dissolution experiment. Only values of $\phi \geq 0.3$ are shown. Once the channel breaks through, it becomes the dominant region of transport.

ity; overall though there is a good agreement between the model and the experiment.

In Fig. 15 from the simulation we observe the appearance of dissolution channels, with a dominant channel formed near the inlet. The location of the simulated channel is similar to the observed channel from the experimental image shown in Fig. 7; this is quantified in Table 4. The appearance of the channel near the inlet reflects the higher initial porosity which focuses most of the flow at both the initial and later stage of the simulation, as the growth of the other channels formed is slower. Injecting a pulse of uniformly distributed particles at the face of the sample and registering their trajectories for $\Delta = 2$ s, we observe that

the channel near the inlet becomes the main medium of transport for the injected particles.

4.3.2. Average dissolution rate

The average effective reaction rate can be defined as

$$r_{\text{eff}} = \frac{\rho_{\text{CaCO}_3}}{M_{\text{CaCO}_3} S_A} \frac{\Delta\phi}{\Delta t}, \quad (21)$$

where $S_A = V_t \sigma_A$ is the sample surface area estimated from the total volume of the simulation domain V_t and specific surface area σ_A . $\Delta\phi$ is the difference in average porosity over a time Δt . In the experiments

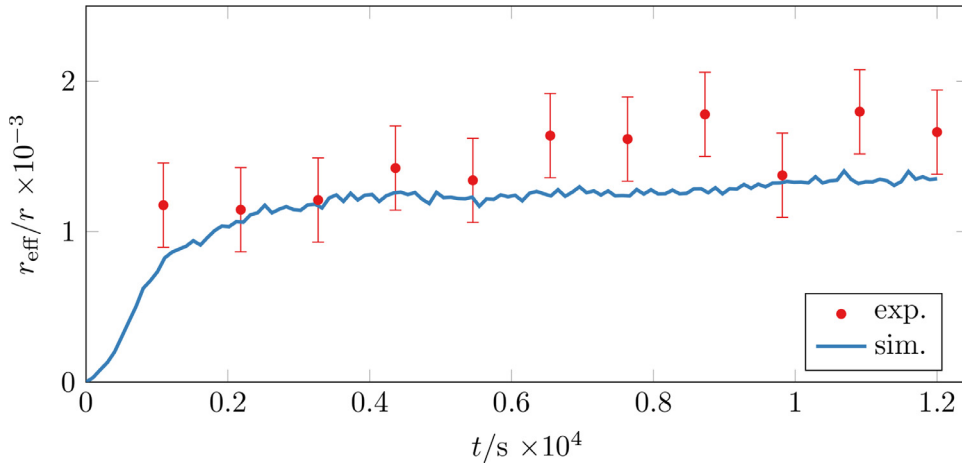


Fig. 16. Experimental and simulated estimated effective dissolution rate. The simulated effective dissolution rate is nearly 780 times smaller than the batch reaction rate while the experimental effective dissolution rate is nearly 680 times smaller than the batch calcite dissolution rate, $r = 8.1 \times 10^{-4} \text{ mol m}^{-2} \text{s}^{-1}$ (Peng et al., 2015). The error bars reflect uncertainty in the experimental measurements.

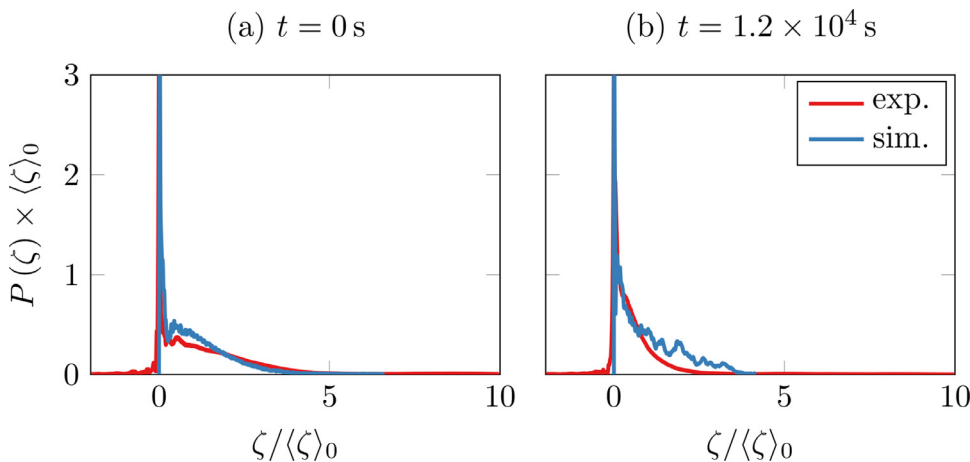


Fig. 17. Particle distribution injected at the core inlet compared against the molecular propagators at (a) 0 s and (b) 1.2×10^4 s. These times represent the dissolution experiment at the beginning and the end.

Δt is the time between measurements, while in the simulation it is the time-step between solutions of the velocity field. Fig. 16 shows the experimental and predicted reaction rates over time: the effective reaction rate averaged over the whole experimental time is approximately $r_{\text{eff}}/r = 1.25 \times 10^{-3}$ for the simulations and $r_{\text{eff}}/r = 1.47 \times 10^{-3}$ for the experiments averaged over the whole time of the process.

The uncertainty in the estimation of reaction rate comes mainly from the conversion of the NMR signal to porosity and calculating porosity changes. We estimate that the measured reaction rate is accurate to within approximately 20%.

These values differ by only 15% showing that the simulations accurately capture the dissolution process to within the uncertainties in the experiment, both on average and throughout the dissolution process, as shown in Fig. 16. However r_{eff} is almost 3 orders of magnitude smaller than the bulk reaction rate r measured without transport limitations (Peng et al., 2015). The reason for this discrepancy is the highly heterogeneous, channelled, flow pattern, which restricts dissolution to only a limited part of the whole rock.

4.3.3. Particle propagators

The propagators or the probability of displacement provides a signature of particle transport. Using the same parameters as before but for non-reactive particles, we simulate a uniform injection at the entry and observe the particle displacements for $\Delta = 2.5 \times 10^{-1}$ s to reflect the same experimental conditions. The results are compared against the experimentally measured propagators and presented in Fig. 17.

When the mean particle velocity is plotted on a log-log scale, as in Fig. 18, we observe that the mean velocity of the particles scales as $v \propto t^{\beta-1}$. This is consistent with the results in Dentz et al. (2004) for $\beta < 1$. Using this relation we estimate an initial average value of $\beta = 0.49$ and the final value of $\beta = 0.64$. The increase of β means that more particles are experiencing a more homogenous flow field within the dissolved dominant channel. Note that these are lower values than $\beta = 0.9$ in each link: here β is an average effective value that accounts for the heterogeneity on scales beyond a single link.

5. Discussion

The porosity field shows the formation of dissolution channels, qualitatively similar to the MRI-derived porosity, as seen in Fig. 15. The mean of the effective reaction rate is almost 3 orders of magnitude smaller than the batch reaction rate (Peng et al., 2015), but in good agreement with the estimated values from the NMR porosity profiles. Previous dissolution experiments at the pore scale showed effective reaction rates that are 10–20 times smaller than the batch reaction rate (Menke et al., 2015; Al-Khulaifi et al., 2017). Here, at a larger scale, transport limitations are even more important, indicating a significant amount of channelling, as evident in the porosity profiles.

Our use of β represents an under-resolved heterogeneity in individual links of the lattice, which is different to the approach of Muljadi et al. (2018) where β varied along slices of the domain, including several links at a time. Additionally, we use the initial porosity distribution of the MRI measurements to build our model, so that the

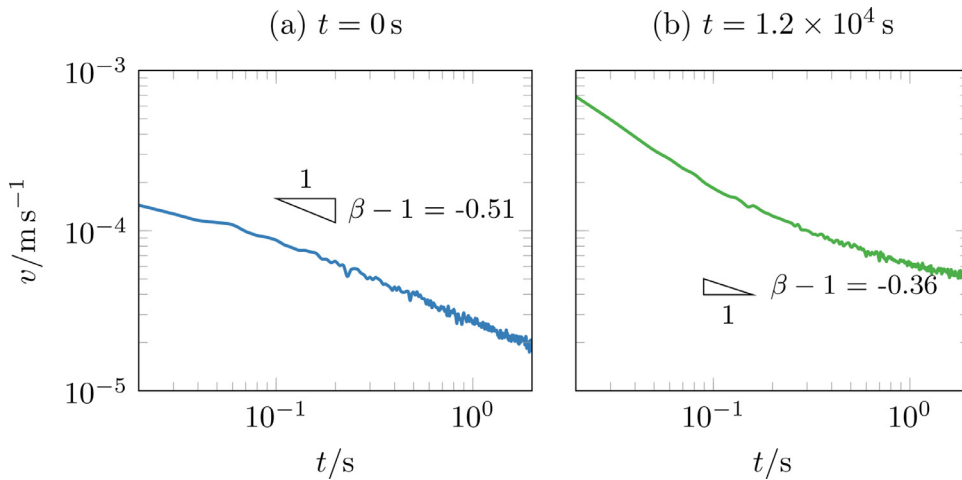


Fig. 18. Particle mean velocity evolution. The graphs show the mean particle velocity along the flow direction $\langle v_x \rangle$ for the domain at the beginning ($t = 0\text{ s}$) and at the end ($t = 1.2 \times 10^4\text{ s}$) of the simulation. As $\langle v \rangle \propto t^{\beta-1}$ we estimate the values of β at the beginning and the end of the simulation as $\beta_{\text{initial}} = 0.49$ and $\beta_{\text{final}} = 0.64$.

emergent propagator distribution is not only dependent on the β parameter but also on the domain heterogeneity as well. The effective, average value of β is lower than value in a link, since it encapsulates the emergent heterogeneity of the medium.

The initial heterogeneity focuses the flow in higher permeability zones, leading to more dissolution in these preferential pathways. This increases the permeability in these regions further, causing more flow focusing and dissolution. The end result is the emergence of a preferential flow channel that carries the vast majority of the flow where reaction is concentrated. The rest of the domain becomes largely stagnant with little flow and reaction — most of the available surface area for reaction does not have access to injected acid leading to a very low overall reaction rate.

6. Conclusions

We developed a CTRW model coupled with a first-order kinetics model to study the dissolution of a Ketton carbonate rock and compared it with experimental NMR measurements.

Our model requires the calibration of a single parameter β which characterizes transport heterogeneity to match the experimental propagator distribution. Having a calibrated initial state, we were able to predict the porosity evolution and the formation of dissolution channels similar to the experimentally-measured channels.

The model is able to qualitatively capture the observed dominant channel from the MRI measurement, and to estimate the effective reaction rate: we estimated an effective reaction rate that was, on average, 780 times lower than the bulk reaction rate without transport limitations; the experiments indicated a ratio of 680. The model is also able to quantitatively reproduce the NMR propagator distribution emerging from the Ketton limestone core sample. Finally, despite using a constant $\beta = 0.9$ value for all links in the model, we calculate an emergent average β from the average velocity of the particles that takes different values both before and after dissolution. We observe that the evolution of the porosity field resulted in a higher emergent β than that before dissolution, because of the dissolution induced heterogeneity change as a result of the flow focusing into preferential channels.

Future work will extend the current model to incorporate mineral heterogeneity and different reaction models.

Declaration of Competing Interest

The authors declare that they have no known competing financial interests or personal relationships that could have appeared to influence the work reported in this paper.

CRediT authorship contribution statement

Rodolfo Oliveira: Conceptualization, Software, Investigation, Writing - original draft, Writing - review & editing. **Branko Bijeljic:** Conceptualization, Supervision, Funding acquisition, Writing - original draft, Writing - review & editing. **Martin J. Blunt:** Conceptualization, Supervision, Writing - original draft, Writing - review & editing. **Adam Colbourne:** Validation. **Andrew J. Sederman:** Methodology, Supervision, Writing - review & editing. **Mick D. Mantle:** Conceptualization, Methodology, Writing - review & editing. **Lynn F. Gladden:** Resources, Supervision.

Acknowledgements

We thank Schlumberger Research for sponsoring the doctoral study during the development of this work and the Engineering and Physical Science Research Council for financial support through grant numbers EP/L012227/1 and EP/L012251/1.

Appendix A. Notes on the probability of displacement

The transition probability p_{ij} from a node i to a node j is defined by

$$p_{ij} = G \frac{\text{Pe}_{ij}}{1 - e^{-\text{Pe}_{ij}}}, \quad \forall v_{ij} > 0 \quad (\text{A.1a})$$

$$p_{ij} = G \frac{\text{Pe}_{ij}}{e^{\text{Pe}_{ij}} - 1}, \quad \forall v_{ij} < 0 \quad (\text{A.1b})$$

where Pe_{ij} is the locally defined Péclet number in the link and G is a normalization factor such that $\sum_j p_{ij} = 1$.

There are cases in which Eq. A.1 can become undefined and will incur numerical errors. Such cases can be avoided with some algebraic manipulation. The two cases explained here are when the velocity is nearly zero or tending to infinity.

Links where the velocity is approximately zero still contribute to the transport of particles. Using a Taylor series expansion at about $\text{Pe} \rightarrow 0$, i.e. $v \rightarrow 0$, reduces Eq. A.1 to

$$\begin{aligned} p_{ij} &= G \frac{\text{Pe}_{ij}}{e^{\text{Pe}_{ij}} - 1} \\ &= G \frac{\text{Pe}_{ij}}{1 + \text{Pe}_{ij} + \mathcal{O}(\text{Pe}_{ij}^2) - 1}, \end{aligned} \quad (\text{A.2})$$

which can be further simplified by ignoring higher order terms into

$$p_{ij} = G, \quad \forall v_{ij} = 0. \quad (\text{A.3})$$

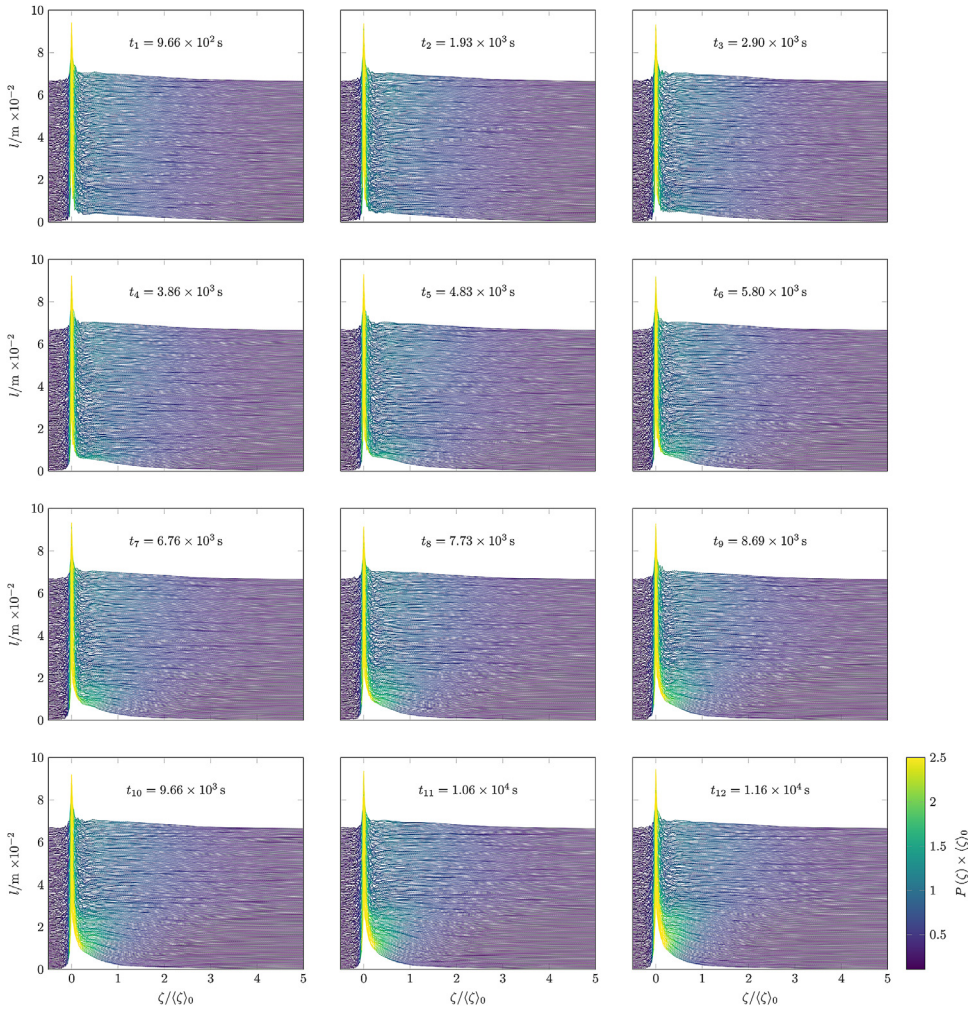


Fig. Appendix B.1. Complete distribution of propagators during the dissolution experiment. The distribution is colour coded to highlight the differences arising from the appearance of dissolution channels. The measurements were taken across the length of the sample $l = 0.072$ m using an observation time $\Delta = 0.25$ s.

On the other hand, when $\text{Pe} \rightarrow \infty$, i.e. $v \rightarrow \infty$, Eq. A.1 reduces to

$$p_{ij} = G\text{Pe}_{ij}, \quad \forall v_{ij} > 0, \quad (\text{A.4a})$$

$$p_{ij} = 0, \quad \forall v_{ij} < 0. \quad (\text{A.4b})$$

Appendix B. Molecular propagator profiles

The experiment was designed to obtain propagator measurements at every 5×10^{-3} m, using an observation time $\Delta = 0.25$ s during the whole dissolution experiment; all the results are shown in Fig. B.1.

References

- Al-Khulaifi, Y., Lin, Q., Blunt, M.J., Bijeljic, B., 2017. Reaction rates in chemically heterogeneous rock: coupled impact of structure and flow properties studied by X-ray microtomography. Environ. Sci. Technol. 51 (7), 4108–4116. <https://doi.org/10.1021/acs.est.6b06224>.
- Al-Khulaifi, Y., Lin, Q., Blunt, M.J., Bijeljic, B., 2018. Reservoir-condition pore-scale imaging of dolomite reaction with supercritical CO₂ acidified brine: effect of pore-structure on reaction rate using velocity distribution analysis. International Journal of Greenhouse Gas Control 68, 99–111. <https://doi.org/10.1016/j.ijggc.2017.11.011>.
- Andrew, M., Bijeljic, B., Blunt, M.J., 2014. Pore-scale imaging of trapped supercritical carbon dioxide in sandstones and carbonates. International Journal of Greenhouse Gas Control 22, 1–14. <https://doi.org/10.1016/j.ijggc.2013.12.018>.
- Aquino, T., Dentz, M., 2017. Chemical continuous time random walks. Phys. Rev. Lett. 119 (23), 230601. <https://doi.org/10.1103/PhysRevLett.119.230601>.
- Bachu, S., 2003. Screening and ranking of sedimentary basins for sequestration of CO₂ in geological media in response to climate change. Environ. Geol. 44 (3), 277–289. <https://doi.org/10.1007/s00254-003-0762-9>.
- Balay, S., Abhyankar, S., Adams, M.F., Brown, J., Brune, P., Buschelman, K., Dalcin, L., Eijkhout, V., Gropp, W.D., Karpeyev, D., Kaushik, D., Knepley, M.G., May, D.A., McInnes, L.C., Mills, R.T., Munson, T., Rupp, K., Sanan, P., Smith, B.F., Zampini, S., Zhang, H., Zhang, H., 2019. PETSc Users Manual. Technical Report ANL-95/11 - Revision 3.11. Argonne National Laboratory.
- Balay, S., Gropp, W.D., McInnes, L.C., Smith, B.F., 1997. Efficient management of parallelism in object oriented numerical software libraries. In: Arge, E., Bruaset, A.M., Langtangen, H.P. (Eds.), Modern Software Tools in Scientific Computing. Birkhäuser Press, pp. 163–202.
- Bear, J., 1972. Dynamics of Fluids in Porous Media. American Elsevier Pub. Co.
- Ben-Zvi, R., Jiang, S., Scher, H., Berkowitz, B., 2019. Finite-element method solution of non-Fickian transport in porous media: the CTRW-FEM package. Groundwater 57 (3), 479–484. <https://doi.org/10.1111/gwat.12813>.
- Ben-Zvi, R., Nissan, A., Scher, H., Berkowitz, B., 2018. A continuous time random walk (CTRW) integro-differential equation with chemical interaction. Eur. Phys. J. B 91 (1), 15. <https://doi.org/10.1140/epjb/e2017-80417-8>.
- Berkowitz, B., Cortis, A., Dentz, M., Scher, H., 2006. Modeling non-Fickian transport in geological formations as a continuous time random walk. Rev. Geophys. 44 (2), RG2003. <https://doi.org/10.1029/2005RG000178>.
- Berkowitz, B., Scher, H., 1997. Anomalous transport in random fracture networks. Phys. Rev. Lett. 79 (20), 4038–4041. <https://doi.org/10.1103/PhysRevLett.79.4038>.
- Berkowitz, B., Scher, H., 2009. Exploring the nature of non-Fickian transport in laboratory experiments. Advances in Water Resources 32 (5), 750–755. <https://doi.org/10.1016/j.advwatres.2008.05.004>.
- Berkowitz, B., Scher, H., Silliman, S.E., 2000. Anomalous transport in laboratory-scale, heterogeneous porous media. Water Resour. Res. 36 (1), 149–158. <https://doi.org/10.1029/1999WR900295>.
- Bijeljic, B., Blunt, M.J., 2006. Pore-scale modeling and continuous time random walk analysis of dispersion in porous media. Water Resour. Res. 42 (1). <https://doi.org/10.1029/2005WR004578>.
- Bijeljic, B., Mostaghimi, P., Blunt, M.J., 2013. Insights into non-Fickian solute transport in carbonates. Water Resour. Res. 49 (5), 2714–2728. <https://doi.org/10.1029/wrcr.20238>.
- Blunt, M.J., Bijeljic, B., Dong, H., Gharbi, O., Iglauer, S., Mostaghimi, P., Paluszny, A., Pentland, C., 2013. Pore-scale imaging and modelling. Advances in Water Resources 51, 197–216. <https://doi.org/10.1016/j.advwatres.2012.03.003>.

- Bos, F.C., Burland, D.M., 1987. Hole transport in polyvinylcarbazole: the vital importance of excitation-light intensity. *Phys. Rev. Lett.* 58 (2), 152–155. <https://doi.org/10.1103/PhysRevLett.58.152>.
- Bruker Almanac, B., 2013. https://www.theresonance.com/wp-content/uploads/2013/02/BrukerAlmanac_Tables.pdf (online, accessed June 12, 2020).
- Callaghan, P.T., 1993. Principles of Nuclear Magnetic Resonance Microscopy. Clarendon Press. reprinted 2011 edition <https://www.worldcat.org/title/principles-of-nuclear-magnetic-resonance-microscopy/oclc/1004245706>
- Chatzis, I., Dullien, F.A.L., 1985. The modeling of mercury porosimetry and the relative permeability of mercury in sandstones using percolation theory. *Int. Chem. Eng. (United States)* 25, 1.
- Choquette, L.C., Pray, P.W.Y., 1970. Geologic nomenclature and classification of porosity in sedimentary carbonates. *Am Assoc Pet Geol.* 54 (2) (2), 207–250.
- Clerke, E.A., 2009. Permeability, relative permeability, microscopic displacement efficiency and pore geometry of M₁ bimodal pore systems in Arab-D limestone. *SPE J* 14 (03), 524–531. <https://doi.org/10.2118/105259-PA>.
- Colbourne, A.A., Sederman, A.J., Mantle, M.D., Gladden, L.F., 2016. Accelerating flow propagator measurements for the investigation of reactive transport in porous media. *Journal of Magnetic Resonance* 272, 68–72. <https://doi.org/10.1016/j.jmr.2016.08.018>.
- Compton, R.G., Pritchard, K.L., Unwin, P.R., 1989. The dissolution of calcite in acid waters: mass transport versus surface control. *Freshwater Biol.* 22 (2), 285–288. <https://doi.org/10.1111/j.1365-2427.1989.tb01101.x>.
- Cotts, R.M., Hoch, M.J.R., Sun, T., Markert, J.T., 1989. Pulsed field gradient stimulated echo methods for improved NMR diffusion measurements in heterogeneous systems. *J. Magn. Reson.* (1969) 83 (2), 252–266. [https://doi.org/10.1016/0022-2364\(89\)90189-3](https://doi.org/10.1016/0022-2364(89)90189-3).
- Daccord, G., Lenormand, R., 1987. Fractal patterns from chemical dissolution. *Nature* 325 (6099), 41–43. <https://doi.org/10.1038/325041a0>.
- Daccord, G., Lenormand, R., Liétard, O., 1993. Chemical dissolution of a porous medium by a reactive fluid-I. Model for the “wormholing” phenomenon. *Chem. Eng. Sci.* 48 (1), 169–178. [https://doi.org/10.1016/0009-2509\(93\)80293-Y](https://doi.org/10.1016/0009-2509(93)80293-Y).
- Daccord, G., Liétard, O., Lenormand, R., 1993. Chemical dissolution of a porous medium by a reactive fluid-II. Convection vs reaction, behavior diagram. *Chemical Engineering Science* 48 (1), 179–186. [https://doi.org/10.1016/0009-2509\(93\)80294-Z](https://doi.org/10.1016/0009-2509(93)80294-Z).
- Daccord, G., Touboul, E., Lenormand, R., 1989. Carbonate Acidizing: Toward a Quantitative Model of the Wormholing Phenomenon. *SPE Production Engineering* 4 (01), 63–68. <https://doi.org/10.2118/16887-PA>.
- Darcy, H., 1856. *Les fontaines publiques de la ville de Dijon. Victor Dalmont, Paris.*
- Dentz, M., Cortis, A., Scher, H., Berkowitz, B., 2004. Time behavior of solute transport in heterogeneous media: transition from anomalous to normal transport. *Advances in Water Resources* 27 (2), 155–173. <https://doi.org/10.1016/j.advwatres.2003.11.002>.
- Detwiler, R.L., Glass, R.J., Bourcier, W.L., 2003. Experimental observations of fracture dissolution: the role of Pecllet number on evolving aperture variability. *Geophys. Res. Lett.* 30 (12). <https://doi.org/10.1029/2003GL017396>.
- Edery, Y., Dror, I., Scher, H., Berkowitz, B., 2015. Anomalous reactive transport in porous media: experiments and modeling. *Phys. Rev. E* 91 (5), 052130. <https://doi.org/10.1103/PhysRevE.91.052130>.
- Edery, Y., Scher, H., Berkowitz, B., 2010. Particle tracking model of bimolecular reactive transport in porous media. *Water Resour. Res.* 46 (7). <https://doi.org/10.1029/2009WR009017>.
- Fanchi, J.R., 2006. *Principles of Applied Reservoir Simulation. Gulf Professional Pub.*
- Fatt, I., 1956. The Network Model of Porous Media. *Petroleum Transactions, AIME* 207, 144–181. <https://www.onepetro.org/general/SPE-574-G>
- Fenwick, D.H., Blunt, M.J., 1998. Three-dimensional modeling of three phase imbibition and drainage. *Advances in Water Resources* 21 (2), 121–143. [https://doi.org/10.1016/S0309-1708\(96\)00037-1](https://doi.org/10.1016/S0309-1708(96)00037-1).
- Fredd, C.N., Fogler, H.S., 1998. Influence of transport and reaction on wormhole formation in porous media. *AIChE J.* 44 (9), 1933–1949. <https://doi.org/10.1002/aic.690440902>.
- Hennig, J., Nauerth, A., Friedburg, H., 1986. RARE imaging: a fast imaging method for clinical MR. *Magn. Reson. Med.* 3 (6), 823–833. <https://doi.org/10.1002/mrm.1910030602>.
- Hoefner, M.L., Fogler, H.S., 1988. Pore evolution and channel formation during flow and reaction in porous media. *AIChE J.* 34 (1), 45–54. <https://doi.org/10.1002/aic.690340107>.
- Hoffman, F., Ronen, D., Pearl, Z., 1996. Evaluation of flow characteristics of a sand column using magnetic resonance imaging. *Journal of Contaminant Hydrology* 22 (1-2), 95–107. [https://doi.org/10.1016/0169-7722\(95\)00079-8](https://doi.org/10.1016/0169-7722(95)00079-8).
- Honari, A., Bijeljic, B., Johns, M.L., May, E.F., 2015. Enhanced gas recovery with CO₂ sequestration: The effect of medium heterogeneity on the dispersion of supercritical CO₂CH₄. *International Journal of Greenhouse Gas Control* 39, 39–50. <https://doi.org/10.1016/j.ijggc.2015.04.014>.
- Kang, P.K., Dentz, M., Le Borgne, T., Juanes, R., 2011. Spatial Markov model of anomalous transport through random lattice networks. *Phys. Rev. Lett.* 107 (18), 180602. <https://doi.org/10.1103/PhysRevLett.107.180602>.
- Karapiperis, T., 1995. Cellular automaton model of precipitation/dissolution coupled with solute transport. *Journal of Statistical Physics* 81 (1-2), 165–180. <https://doi.org/10.1007/BF02179974>.
- Kenney, J.P.L., Kirby, M.E., Cuadros, J., Weiss, D.J., 2017. A conceptual model to predict uranium removal from aqueous solutions in waterrock systems associated with low- and intermediate-level radioactive waste disposal. *RSC Advances* 7 (13), 7876–7884. <https://doi.org/10.1039/C6RA26773D>.
- Kolmogorov, A.N., 1933. Sulla determinazione empirica di una legge di distribuzione. *Giorn. Inst. Italiano Attuari* 4, 83–91.
- Le Borgne, T., Dentz, M., Carrera, J., 2008. Spatial Markov processes for modeling Lagrangian particle dynamics in heterogeneous porous media. *Physical Review E- Statistical, Nonlinear, and Soft Matter Physics* 78 (2), 026308. <https://doi.org/10.1103/PhysRevE.78.026308>.
- Levy, M., Berkowitz, B., 2003. Measurement and analysis of non-Fickian dispersion in heterogeneous porous media. *Journal of Contaminant Hydrology* 64 (3-4), 203–226. [https://doi.org/10.1016/S0169-7722\(02\)00204-8](https://doi.org/10.1016/S0169-7722(02)00204-8).
- Lin, Q., Al-Khalafi, Y., Blunt, M.J., Bijeljic, B., 2016. Quantification of sub-resolution porosity in carbonate rocks by applying high-salinity contrast brine using X-ray microtomography differential imaging. *Advances in Water Resources* 96, 306–322. <https://doi.org/10.1016/j.advwatres.2016.08.002>.
- Liu, M., Mostaghimi, P., 2018. Numerical simulation of fluid-fluid-solid reactions in porous media. *International Journal of Heat and Mass Transfer* 120, 194–201. <https://doi.org/10.1016/j.ijheatmasstransfer.2017.11.141>.
- Mahmoud, M., Barri, A., Elkhatatny, S., 2017. Mixing chelating agents with seawater for acid stimulation treatments in carbonate reservoirs. *Journal of Petroleum Science and Engineering* 152, 9–20. <https://doi.org/10.1016/j.petrol.2017.02.005>.
- Meakin, P., Tartakovsky, A.M., 2009. Modeling and simulation of pore-scale multiphase fluid flow and reactive transport in fractured and porous media. *Rev. Geophys.* 47 (3), RG3002. <https://doi.org/10.1029/2008RG002633>.
- Menke, H.P., Andrew, M.G., Blunt, M.J., Bijeljic, B., 2016. Reservoir condition imaging of reactive transport in heterogeneous carbonates using fast synchrotron tomography - Effect of initial pore structure and flow conditions. *Chem. Geol.* 428, 15–26. <https://doi.org/10.1016/j.chemgeo.2016.02.030>.
- Menke, H.P., Bijeljic, B., Andrew, M.G., Blunt, M.J., 2015. Dynamic Three-Dimensional Pore-Scale Imaging of Reaction in a Carbonate at Reservoir Conditions. *Environ. Sci. Technol.* 49 (7), 4407–4414. <https://doi.org/10.1021/es505789f>.
- Menke, H.P., Reynolds, C.A., Andrew, M.G., Pereira Nunes, J.P., Bijeljic, B., Blunt, M.J., 2018. 4D multi-scale imaging of reactive flow in carbonates: Assessing the impact of heterogeneity on dissolution regimes using streamlines at multiple length scales. *Chemical Geology* 481, 27–37. <https://doi.org/10.1016/j.chemgeo.2018.01.016>.
- Metz, B., Davidson, O., de Coninck, H., Loos, M., Meyer, L., 2010. Carbon Dioxide Capture and Storage. Technical Report. IPCC, Geneva, Switzerland. <http://www.ncbi.nlm.nih.gov/pubmed/20698658>
- Mitchell, J., Sederman, A.J., Fordham, E.J., Johns, M.L., Gladden, L.F., 2008. A rapid measurement of flow propagators in porous rocks. *Journal of Magnetic Resonance* 191 (2), 267–272. <https://doi.org/10.1016/j.jmr.2007.12.014>.
- Molins, S., Trebotich, D., Steefel, C.I., Shen, C., 2012. An investigation of the effect of pore scale flow on average geochemical reaction rates using direct numerical simulation. *Water Resour. Res.* 48 (3). <https://doi.org/10.1029/2011WR011404>.
- Montroll, E.W., Scher, H., 1973. Random walks on lattices. IV. Continuous-time walks and influence of absorbing boundaries. *J. Stat. Phys.* 9 (2), 101–135. <https://doi.org/10.1007/BF01016843>.
- Montroll, E.W.W., Weiss, G.H.G.H., 1965. Random walks on lattices. II. *J. Math. Phys.* 6 (2), 167–181. <https://doi.org/10.1063/1.1704269>.
- Muljadi, B.P., Bijeljic, B., Blunt, M.J., Colbourne, A., Sederman, A.J., Mantle, M.D., Gladden, L.F., 2018. Modelling and upscaling of transport in carbonates during dissolution: Validation and calibration with NMR experiments. *Journal of Contaminant Hydrology* 212, 85–95. <https://doi.org/10.1016/j.jconhyd.2017.08.008>.
- Nierode, D.E., Williams, B.B., 1971. Characteristics of acid reaction in limestone formations. *Soc Pet Eng J* 11 (4), 406–418. <https://doi.org/10.2118/3101-PA>.
- Oliveira, T.D.S., Blunt, M.J., Bijeljic, B., 2019. Modelling of multispecies reactive transport on pore-space images. *Advances in Water Resources* 127, 192–208. <https://doi.org/10.1016/j.advwatres.2019.03.012>.
- Oswald, S., Kinzelbach, W., Greiner, A., Brix, G., 1997. Observation of flow and transport processes in artificial porous media via magnetic resonance imaging in three dimensions. *Geoderma* 80 (3-4), 417–429. [https://doi.org/10.1016/S0016-7061\(97\)00064-5](https://doi.org/10.1016/S0016-7061(97)00064-5).
- Paulsen, J.L., Cho, H., Cho, G., Song, Y.Q., 2011. Acceleration of multi-dimensional propagator measurements with compressed sensing. *Journal of Magnetic Resonance* 213 (1), 166–170. <https://doi.org/10.1016/j.jmr.2011.08.025>.
- Peng, C., Anabaraonye, B.U., Crawshaw, J.P., Maitland, G.C., Trusler, J.P.M., 2016. Kinetics of carbonate mineral dissolution in CO₂-acidified brines at storage reservoir conditions. *Faraday Discussions* 192 (0), 545–560. <https://doi.org/10.1039/C6FD00048G>.
- Peng, C., Crawshaw, J.P., Maitland, G.C., Trusler, J.P.P.M., 2015. Kinetics of calcite dissolution in CO₂-saturated water at temperatures between (323 and 373) K and pressures up to 13.8 MPa. *Chemical Geology* 403, 74–85. <https://doi.org/10.1016/j.chemgeo.2015.03.012>.
- Pereira Nunes, J.A.P., Bijeljic, B., Blunt, M.J., 2016. Pore-space structure and average dissolution rates: a simulation study. *Water Resour. Res.* 52 (9), 7198–7212. <https://doi.org/10.1002/2016WR019313>.
- Pereira Nunes, J.A.P., Blunt, M.J., Bijeljic, B., 2016. Pore-scale simulation of carbonate dissolution in micro-CT images. *J. Geophys. Res.* 121 (2), 558–576. <https://doi.org/10.1002/2015JB012117>.
- Plummer, L.N., Wigley, T.M.L., Parkhurst, D.L., 1978. The kinetics of calcite dissolution in CO₂-water systems at 5 degrees to 60 degrees C and 0.0 to 1.0 atm CO₂. *Am J Sci* 278 (2), 179–216. <https://doi.org/10.2475/ajs.278.2.179>.
- Raeini, A.Q., Bijeljic, B., Blunt, M.J., 2018. Generalized network modeling of capillary-dominated two-phase flow. *Phys. Rev. E* 97 (2), 023308. <https://doi.org/10.1103/PhysRevE.97.023308>.
- Ramskill, N.P., Bush, I., Sederman, A.J., Mantle, M.D., Benning, M., Anger, B.C., Appel, M., Gladden, L.F., 2016. Fast imaging of laboratory core floods using 3D compressed sensing RARE MRI. *Journal of Magnetic Resonance* 270, 187–197. <https://doi.org/10.1016/j.jmr.2016.07.017>.

- Ramskill, N.P., Sederman, A.J., Mantle, M.D., Appel, M., de Jong, H., Gladden, L.F., 2018. In situ chemically-selective monitoring of multiphase displacement processes in a carbonate rock using 3D magnetic resonance imaging. *Transp. Porous Media* 121 (1), 15–35. <https://doi.org/10.1007/s11242-017-0945-6>.
- Raoof, A., Nick, H.M., Hassanzadeh, S.M., Spiers, C.J., 2013. PoreFlow: a complex pore-network model for simulation of reactive transport in variably saturated porous media. *Computers & Geosciences* 61, 160–174. <https://doi.org/10.1016/J.CAGEO.2013.08.005>.
- Rhodes, M.E., Bijeljic, B., Blunt, M.J., 2008. Pore-to-field simulation of single-phase transport using continuous time random walks. *Advances in Water Resources* 31 (12), 1527–1539. <https://doi.org/10.1016/j.advwatres.2008.04.006>.
- Rhodes, M.E., Bijeljic, B., Blunt, M.J., 2009. A rigorous pore-to-field-scale simulation method for single-phase flow based on continuous-time random walks. *SPE J.* 14 (01), 88–94. <https://doi.org/10.2118/106434-PA>.
- Rhodes, M.E., Blunt, M.J., 2006. An exact particle tracking algorithm for advective-dispersive transport in networks with complete mixing at nodes. *Water Resour. Res.* 42 (4). <https://doi.org/10.1029/2005WR004504>.
- Ribeiro, A.C.F., Barros, M.C.F., Teles, A.S.N., Valente, A.J.M., Lobo, V.M.M., Sobral, A.J.F.N., Esteso, M.A., 2008. Diffusion coefficients and electrical conductivities for calcium chloride aqueous solutions at 298.15K and 310.15K. *Electrochimica Acta* 54 (2), 192–196. <https://doi.org/10.1016/j.electacta.2008.08.011>.
- Saad, Y., Schultz, M.H., 1986. GMRES: a generalized minimal residual algorithm for solving nonsymmetric linear systems. *SIAM J. Sci. Stat.Comput.* 7 (3), 856–869. <https://doi.org/10.1137/0907058>.
- Scher, H., Lax, M., 1973. Stochastic transport in a disordered solid. I. Theory. *Phys Rev B* 7 (10), 4491–4502. <https://doi.org/10.1103/PhysRevB.7.4491>.
- Scher, H., Lax, M., 1973. Stochastic transport in a disordered solid. II. Impurity conduction. *Phys Rev B* 7 (10), 4502–4519. <https://doi.org/10.1103/PhysRevB.7.4502>.
- Scher, H., Montröll, E.W., 1975. Anomalous transit-time dispersion in amorphous solids. *Phys Rev B* 12 (6), 2455–2477. <https://doi.org/10.1103/PhysRevB.12.2455>.
- Scheven, U.M., Seland, J.G., Cory, D.G., 2005. NMR-propagator measurements in porous media in the presence of surface relaxation and internal fields. *Magnetic Resonance Imaging* 23 (2 SPEC. ISS.), 363–365. <https://doi.org/10.1016/j.mri.2004.11.054>.
- Scheven, U.M., Verganelakis, D., Harris, R., Johns, M.L., Gladden, L.F., 2005. Quantitative nuclear magnetic resonance measurements of preasymptotic dispersion in flow through porous media. *Phys. Fluids* 17 (11), 117107. <https://doi.org/10.1063/1.2131871>.
- Seymour, J.D., Callaghan, P.T., 1997. Generalized approach to NMR analysis of flow and dispersion in porous media. *AIChE J.* 43 (8), 2096–2111. <https://doi.org/10.1002/aic.690430817>.
- Singh, K., Anabaraonye, B.U., Blunt, M.J., Crawshaw, J., 2018. Partial dissolution of carbonate rock grains during reactive CO₂-saturated brine injection under reservoir conditions. *Adv. Water Resour.* 122, 27–36. <https://doi.org/10.1016/j.advwatres.2018.09.005>.
- Smirnov, N.V., 1939. Estimate of deviation between empirical distribution functions in two independent samples. *Bull. Moscow Univ. 2*, 3–16.
- Sochi, T., Blunt, M.J., 2008. Pore-scale network modeling of Ellis and Herschel-Bulkley fluids. *J. Pet. Sci. Eng.* 60 (2), 105–124. <https://doi.org/10.1016/j.petrol.2007.05.009>.
- Szymczak, P., Ladd, A.J.C., 2012. Reactive-infiltration instabilities in rocks. Fracture dissolution. *J. Fluid Mech.* 702, 239–264. <https://doi.org/10.1017/jfm.2012.174>.
- Tansey, J., Balhoff, M.T., 2016. Pore network modeling of reactive transport and dissolution in porous media. *Transp. Porous Media* 113 (2), 303–327. <https://doi.org/10.1007/s11242-016-0695-x>.
- Terra, G.J.S., Spadini, A.R., França, A.B., Sombra, C.L., Zambonato, E.E., Juschkak, L.C.d.S., Arienti, L.M., Erthal, M.M., Blauth, M., Franco, M.P., Matsuda, N.S., da Silva, N.G.C., Moretti, P., D'Avila, R.S.F., de Souza, R.S., Tonietto, S., dos Anjos, S.M.C., Campinho, V.S., Winter, W.R., 2010. Classificação de rochas carbonáticas aplicável às bacias sedimentares brasileiras. *Boletim de Geociências - Petrobras* 18 (1), 9–29. <http://vdpf.petrobras.com.br/vdpf/PDFHighlightServlet.svl?acao=pdf&codigoArtigo=3673>
- Tian, Z., Wang, J., 2018. Lattice Boltzmann simulation of dissolution-induced changes in permeability and porosity in 3D CO₂ reactive transport. *J. Hydrol.* 557, 276–290. <https://doi.org/10.1016/j.jhydrol.2017.12.037>.
- Tiedje, T., 1984. Chapter 6 information about band-tail states from time-of-flight experiments. In: *Semiconductors and Semimetals*, Vol. 21. Elsevier, pp. 207–238. [https://doi.org/10.1016/S0080-8784\(08\)63070-7](https://doi.org/10.1016/S0080-8784(08)63070-7).
- Valvatne, P.H., Blunt, M.J., 2004. Predictive pore-scale modeling of two-phase flow in mixed wet media. *Water Resour. Res.* 40 (7). <https://doi.org/10.1029/2003WR002627>.
- Wildenschild, D., Sheppard, A.P., 2013. X-ray imaging and analysis techniques for quantifying pore-scale structure and processes in subsurface porous medium systems. *Advances in Water Resources* 51, 217–246. <https://doi.org/10.1016/j.advwatres.2012.07.018>.
- Xu, L., Szymczak, P., Toussaint, R., Flekkøy, E.G., Måløy, K.J., 2020. Dissolution phase diagram in radial geometry. *Frontiers in Physics* 8, 369. <https://doi.org/10.3389/fphy.2020.00369>.